Anisotropy of spin relaxation and transverse transport in metals

2013 J. Phys.: Condens. Matter 25 163201

(http://iopscience.iop.org/0953-8984/25/16/163201)

J. Phys.: Condens. Matter **25** (2013) 163201 (24pp) doi:10.1088/0953-8984/25/16/163201

TOPICAL REVIEW

Anisotropy of spin relaxation and transverse transport in metals

Yuriy Mokrousov[1], Hongbin Zhang[1], Frank Freimuth[1], Bernd Zimmermann[1], Nguyen H Long[1], Jürgen Weischenberg[1], Ivo Souza[2,3], Phivos Mavropoulos[1] and Stefan Blügel[1]

[1] Peter Grünberg Institut and Institute for Advanced Simulation, Forschungszentrum Jülich and JARA, D-52425 Jülich, Germany
[2] Centro de Física de Materiales (CSIC) and DIPC, Universidad del País Vasco, 20018 San Sebastián, Spain
[3] Ikerbasque Foundation, 48011 Bilbao, Spain

E-mail: y.mokrousov@fz-juelich.de

Received 7 November 2012, in final form 15 February 2013
Published 20 March 2013
Online at stacks.iop.org/JPhysCM/25/163201

Abstract
Using first-principles methods we explore the anisotropy of the spin relaxation and transverse transport properties in bulk metals with respect to the real-space direction of the spin-quantization axis in paramagnets or of the spontaneous magnetization in ferromagnets. Owing to the presence of the spin–orbit coupling the orbital and spin character of the Bloch states depends sensitively on the orientation of the spins relative to the crystal axes. This leads to drastic changes in quantities which rely on interband mixing induced by the spin–orbit interaction. The anisotropy is particularly striking for quantities which exhibit spiky and irregular distributions in the Brillouin zone, such as the spin-mixing parameter or the Berry curvature of the electronic states. We demonstrate this for three cases: (i) the Elliott–Yafet spin-relaxation mechanism in paramagnets with structural inversion symmetry; (ii) the intrinsic anomalous Hall effect in ferromagnets; and (iii) the spin Hall effect in paramagnets. We discuss the consequences of the pronounced anisotropic behavior displayed by these properties for spin-polarized transport applications.

(Some figures may appear in colour only in the online journal)

Contents

1. Introduction

Phenomena belonging to the field of spintronics are associated with the spin of electrons, which do the job of carrying

information across a device. In such a situation, the fact that the spin and orbital degrees of freedom of Bloch electrons in a solid are fundamentally related due to the presence of spin–orbit coupling (SOC) becomes of great importance. Normally, the spin–orbit interaction can be considered as a small perturbation compared to the other relevant energy scales for electrons in a crystal (such as band gaps, band widths, or exchange splittings). Its influence is to mix in a non-trivial fashion the spin and orbital character of the Bloch states at each crystal momentum. If we consider now the non-equilibrium situation of an electron moving in one of the Bloch bands across the crystal under the influence of an external electric field, the spin–orbit mediated interaction with other Bloch states will determine its spin and orbital dynamics. Consider the case of a paramagnetic crystal. If we manage to make our initial incoming electron spin-polarized—a typical situation in a spin-injection experiment—this spin polarization will decrease in time due to random scattering off impurities or phonons [1, 2], until it completely vanishes. Its exponential decay in time is characterized by the *spin-relaxation time*, which serves as one of the most basic material parameters in spintronics [3]. In another example, the presence of the spin–orbit coupling modifies in a subtle way the dynamics of Bloch electrons under an applied electric field by adding a spin-dependent transverse component to the velocity. This will result in an *anomalous Hall effect* (AHE) in ferromagnets [4], and a *spin Hall effect* (SHE) in paramagnets [5]. Conceptually, the understanding of these two phenomena over the past 10–15 years has generated a number of novel concepts in modern spintronics, and solid state physics in general. While practically the AHE and SHE have entered the everyday toolkit in experimental spintronics, further exciting research in this field is still ahead of us. A lot remains to be done concerning the microscopic understanding and first-principles description of spin-relaxation phenomena and transverse transport properties in real materials.

The crystal field in a solid is manifestly anisotropic and lifts the degeneracy between states of different magnetic quantum numbers. Together with the action of SOC, this results in a strong dependence of the spin and orbital character of the Bloch states on the choice of the spin-quantization axis (SQA) or the direction of the magnetization in the crystal, since the matrix elements of the orbital angular momentum operator are strongly anisotropic themselves. In ferromagnets, crystal field splitting combined with the anisotropy of the orbital angular momentum operator leads to a dependence of the band energy on the direction of the magnetization, resulting in the magneto-crystalline anisotropy energy [6–8]—one of the fundamental characteristics of magnetic materials. In the field of transport phenomena in metals, the anisotropy of the electronic structure with respect to the magnetization direction leads to such prominent phenomena as anisotropic magnetoresistance [9], tunneling anisotropic magnetoresistance [10, 11] and ballistic anisotropic magnetoresistance [12]. As in the case of the magneto-crystalline anisotropy energy, these effects can already be captured in many cases by considering only the changes in the band topology in the Brillouin zone as the orientation of the magnetization is varied [10, 12–14]. This situation is in contrast to the case of the AHE and SHE, which are often governed by band degeneracies at the Fermi level [15]. In this case the dependence of the eigenenergies on the global SQA or magnetization direction in real space is either absent or can often be neglected, while the anisotropy of the spin and orbital resolution of the wavefunctions becomes of primary importance, and could lead to very large values of the anisotropy of the Hall conductivities, as speculated already by Fivaz in 1969 for the anomalous Hall effect [16].

The significant anisotropy of the spin-relaxation and Hall effects is a valuable tool for tuning the transport properties of spintronics devices. Since such anisotropy is an intrinsic property of the crystalline solid, it should be properly averaged when using polycrystalline samples, as well as when considering the effect of temperature and magnetization dynamics on the measured spin polarization or transverse current [17]. Experimentally, only the anisotropy of the anomalous Hall effect with respect to the direction of the magnetization in the sample has been researched in the past and in many cases a very large anisotropy was found [18–25], while evidence of anisotropy in the spin Hall effect [26] and spin relaxation has been presented only recently [27, 28].

Here, we review the current theoretical understanding of the three phenomena occurring in perfect crystals: (i) anisotropy of the spin relaxation with respect to the choice of the real-space SQA determined by an applied magnetic field or spin polarization of injected electrons, (ii) anisotropy of the intrinsic anomalous Hall effect with respect to the real-space direction of the saturation magnetization in ferromagnets, and (iii) anisotropy of the intrinsic spin Hall effect with respect to the choice of the SQA in real space, defined by the direction of the spin polarization of the spin current (figure 1). We focus on the developments which have taken place over the past few years [17, 31–36]. We present arguments and show from first-principles calculations that due to the sensitivity of spin-relaxation and Hall effects to the SOC-mediated coupling between (nearly) degenerate states in the vicinity of the Fermi level, the anisotropy of these effects can be gigantic, and has in principle no theoretical limit. Manifestly, for some directions of the SQA and magnetization in the crystal the spin-relaxation rates and Hall currents can be suppressed by orders of magnitude, or even display a change of sign in corresponding conductivity components. We discuss possible applications of such large anisotropies, encourage further experimental studies in this area, and emphasize that a wide range of materials exhibit anisotropic transverse transport and spin relaxation, from bulk solids to surfaces and interfaces with essentially lowered lattice symmetry.

The review is structured as follows. The rest of this section is dedicated to a brief introduction to the Elliott–Yafet [1, 2] spin-relaxation mechanism and the intrinsic anomalous and spin Hall effects in solids. In section 2 we describe the computational methods and provide the details of first-principles calculations presented in the rest of the review. The concept of anisotropic Elliott–Yafet spin relaxation is introduced and discussed in detail both from

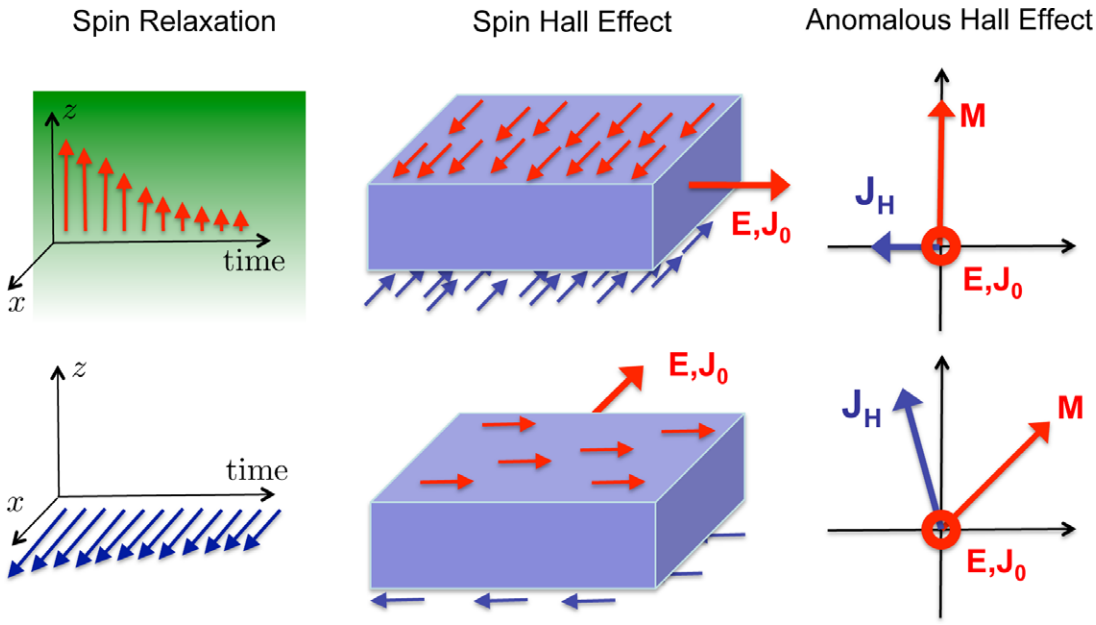

Figure 1. Setup of the anisotropic spin-relaxation and transverse spin and anomalous Hall effects in metals. *Anisotropic spin relaxation* (left): an electron with a certain direction of spin, injected into a solid which exhibits anisotropic spin relaxation, will lose the memory of its initial spin polarization over a period of time, which depends on the direction of the spin polarization in real space (z or x, red and blue arrows correspondingly). *Anisotropic spin Hall effect* (middle): the magnitude of the spin current and the direction of its spin polarization (related to the sign and magnitude of the spin accumulation on the surfaces of the sample) measured along a certain direction in a crystal depends on the direction of applied electric field $\mathbf{E}$ which generates the longitudinal electric current $\mathbf{J}_0$. *Anisotropic anomalous Hall effect* (right): for a fixed direction of applied electric field $\mathbf{E}$ and corresponding longitudinal electric current $\mathbf{J}_0$ (pointing in the z direction out of the plane of the figure), the direction and magnitude of the Hall current $\mathbf{J}_\mathrm{H}$ depend on the direction of magnetization $\mathbf{M}$ in the sample. Note that for a general direction of $\mathbf{M}$ away from high-symmetry axes in the crystal, $\mathbf{J}_\mathrm{H}$ can be non-orthogonal to $\mathbf{M}$.

model and *ab initio* viewpoints in section 3. Sections 4 and 5 are dedicated to anisotropic intrinsic spin and anomalous Hall effects in transition metals and their alloys, respectively. We conclude the review and provide an outlook in section 6.

Throughout the text we shall make frequent use of the following abbreviations. AHC: anomalous Hall conductivity; AHE: anomalous Hall effect; EYP: Elliott–Yafet parameter; PHE: planar Hall effect; SHC: spin Hall conductivity; SHE: spin Hall effect; SOC: spin–orbit coupling; SQA: spin-quantization axis.

1.1. Spin relaxation in paramagnets

As a first example of a situation in which the importance of the anisotropy of the wavefunctions with respect to the choice of the spin-quantization axis is very pronounced we consider the phenomenon of spin relaxation. To be concrete, here we concentrate on the Elliott–Yafet spin-relaxation mechanism, dominant in materials with structural bulk inversion symmetry [1, 2], which is due to scattering of electrons off phonons or impurities. Owing to the presence of spin–orbit coupling in the system such scattering events will flip the spin of the electron with a certain probability, which depends on both the wavefunctions of the ideal crystal and the scattering potential. However, according to the Elliott approximation [1], a reasonable estimate of the ratio between momentum- and spin-relaxation times, T_p and T_1, can be given by neglecting the form of the scattering potential as follows: $T_\mathrm{p}/T_1 \approx 4b^2$, where b^2 is the Elliott–Yafet parameter (EYP) defined below, which is an intrinsic property of the ideal crystal [37].

The coexistence of time-reversal and space inversion symmetries implies that the eigenenergies of the crystal at any given Bloch momentum $\mathbf{k}$ are at least two-fold degenerate. Following Elliott, we write the corresponding states as superpositions of the form

$$\psi^{\uparrow}_{\mathbf{k}\hat{\mathbf{s}}}(\mathbf{r}) = \left[a_{\mathbf{k}\hat{\mathbf{s}}}(\mathbf{r})|\uparrow\rangle_{\hat{\mathbf{s}}} + b_{\mathbf{k}\hat{\mathbf{s}}}(\mathbf{r})|\downarrow\rangle_{\hat{\mathbf{s}}}\right] \mathrm{e}^{\mathrm{i}\mathbf{k}\cdot\mathbf{r}}, \tag{1}$$

$$\psi^{\downarrow}_{\mathbf{k}\hat{\mathbf{s}}}(\mathbf{r}) = \left[a^*_{-\mathbf{k}\hat{\mathbf{s}}}(\mathbf{r})|\downarrow\rangle_{\hat{\mathbf{s}}} - b^*_{-\mathbf{k}\hat{\mathbf{s}}}(\mathbf{r})|\uparrow\rangle_{\hat{\mathbf{s}}}\right] \mathrm{e}^{\mathrm{i}\mathbf{k}\cdot\mathbf{r}}. \tag{2}$$

The two spin states $|\uparrow\rangle_{\hat{\mathbf{s}}}$ and $|\downarrow\rangle_{\hat{\mathbf{s}}}$ are eigenstates of $\hat{\mathbf{s}}\cdot\mathbf{S}$, where $\hat{\mathbf{s}}$ is the unit vector along the chosen SQA, $\mathbf{S} = \frac{\hbar}{2}\boldsymbol{\tau}$ is the spin angular momentum operator, and $\boldsymbol{\tau}$ are the Pauli matrices. Here, we have adopted a notation that allows us to vary the spin and angular momentum quantization axis $\hat{\mathbf{s}}$, which is useful for a description of the anisotropy, whereas usually one meets the above equations with $\hat{\mathbf{s}}$ being implied along the z-axis. So, for example, $|\uparrow\rangle_z$ and $|\downarrow\rangle_z$ are the eigenstates of the S_z operator. More generally, the reference frame is specified by the SQA direction $\hat{\mathbf{s}}$, which is chosen to coincide with the polarization direction of the initial/injected spin population. The functions $a_{\mathbf{k}\hat{\mathbf{s}}}(\mathbf{r})$ and $b_{\mathbf{k}\hat{\mathbf{s}}}(\mathbf{r})$ exhibit the periodicity of the crystal lattice, and we define $b^2_{\mathbf{k}\hat{\mathbf{s}}}$ as the unit cell integral $\int_{\mathrm{u.c.}} \mathrm{d}^3r\,|b_{\mathbf{k}\hat{\mathbf{s}}}(\mathbf{r})|^2$ (similarly for $a^2_{\mathbf{k}\hat{\mathbf{s}}}$, which satisfies $a^2_{\mathbf{k}\hat{\mathbf{s}}} = 1 - b^2_{\mathbf{k}\hat{\mathbf{s}}}$).

For fixed $\hat{\mathbf{s}}$, the degenerate $\psi^{\uparrow}_{\mathbf{k}\hat{\mathbf{s}}}$ and $\psi^{\downarrow}_{\mathbf{k}\hat{\mathbf{s}}}$ states (and the corresponding $a_{\mathbf{k}\hat{\mathbf{s}}}(\mathbf{r})$ and $b_{\mathbf{k}\hat{\mathbf{s}}}(\mathbf{r})$) can be chosen, via a linear combination, such that the spin-expectation value $S_{\mathbf{k}\hat{\mathbf{s}}} = \langle\psi^{\uparrow}|S_{\hat{\mathbf{s}}}|\psi^{\uparrow}\rangle$ is maximal. The spin-mixing parameter is then given by $b^2_{\mathbf{k}\hat{\mathbf{s}}} = 1/2 - S_{\mathbf{k}\hat{\mathbf{s}}}/\hbar$, and is usually small, due to the weakness of the SOC. In this case the Bloch states are of nearly pure spin character. (Thus, $a_{\mathbf{k}\hat{\mathbf{s}}}$ represents the 'large' component of the spinor, while $b_{\mathbf{k}\hat{\mathbf{s}}}$ is the 'small' component. The relation between the large or small components of $\psi^{\uparrow}_{\mathbf{k}\hat{\mathbf{s}}}$ and $\psi^{\downarrow}_{\mathbf{k}\hat{\mathbf{s}}}$, $a_{\mathbf{k}\hat{\mathbf{s}}} = a^*_{-\mathbf{k}\hat{\mathbf{s}}}$ and $b_{\mathbf{k}\hat{\mathbf{s}}} = b^*_{-\mathbf{k}\hat{\mathbf{s}}}$, follows from space and time inversion symmetry.) However, at special spin-flip hot-spot points in the band structure, e.g. accidental degeneracies, Brillouin zone boundaries or other high-symmetry points [37], $b^2_{\mathbf{k}\hat{\mathbf{s}}}$ may increase significantly up to a value of $\frac{1}{2}$, which corresponds to the case of fully spin-mixed states. Generally, the distribution of the spin-mixing parameter for a metal with a complicated Fermi surface can be far from trivial. The Fermi-surface averaged Elliott–Yafet parameter is given by

$$b^2_{\hat{\mathbf{s}}} = \frac{1}{n(E_{\mathrm{F}})}\frac{1}{\hbar}\int_{\mathrm{FS}}\frac{b^2_{\mathbf{k}\hat{\mathbf{s}}}}{|\mathbf{v}_{\mathrm{F}}(\mathbf{k})|}\,\mathrm{d}^2k, \tag{3}$$

where $\mathbf{v}_{\mathrm{F}}(\mathbf{k})$ is the Fermi velocity. The normalization by the density of states at the Fermi level, $n(E_{\mathrm{F}}) = 1/\hbar\int_{\mathrm{FS}}|\mathbf{v}_{\mathrm{F}}(\mathbf{k})|^{-1}\,\mathrm{d}^2k$, ensures that $0 \le b^2_{\hat{\mathbf{s}}} \le \frac{1}{2}$.

For the ensuing discussion it will be useful to divide the spin–orbit operator into spin-conserving and spin-flip parts, $\xi(LS^{\uparrow\uparrow})$ and $\xi(LS^{\uparrow\downarrow})$, given respectively by the first and second terms of the following expression [32]:

$$\xi\mathbf{L}\cdot\mathbf{S} = \xi L_{\hat{\mathbf{s}}}S_{\hat{\mathbf{s}}} + \xi\left(L^+_{\hat{\mathbf{s}}}S^-_{\hat{\mathbf{s}}} + L^-_{\hat{\mathbf{s}}}S^+_{\hat{\mathbf{s}}}\right)/2. \tag{4}$$

Here ξ is the spin–orbit coupling strength, $\mathbf{L}$ is the operator of the orbital angular momentum, $L_{\hat{\mathbf{s}}} = \mathbf{L}\cdot\hat{\mathbf{s}}$, $S_{\hat{\mathbf{s}}} = \mathbf{S}\cdot\hat{\mathbf{s}}$, and $L^{\pm}_{\hat{\mathbf{s}}}$ and $S^{\pm}_{\hat{\mathbf{s}}}$ are the raising and lowering operators for orbital and spin angular momenta in the reference frame defined by the SQA $\hat{\mathbf{s}}$. Acting on a state of the crystal obtained without SOC, the spin-flip part of the SOC can flip its spin, while the spin-conserving part will keep it intact. It is clear that the dot product $\mathbf{L}\cdot\mathbf{S}$ is independent of $\hat{\mathbf{s}}$, leaving the eigenenergies of the Hamiltonian invariant if $\hat{\mathbf{s}}$ is rotated. However, the spin-conserving and spin-flip parts, separately, depend on the choice of the SQA. In ferromagnets, the spin-conserving part of SOC is the one which is largely responsible for the values of the magneto-crystalline anisotropy energy and orbital moments [7, 8]. In paramagnets, the Elliott–Yafet spin-relaxation mechanism is driven by the spin-flip part of the SOC.

In an experiment, the spin polarization of the electrons subject to spin relaxation is defined by the direction of the external magnetic field (e.g. in conduction-electron spin resonance experiments) or by the polarization of ferromagnetic leads (e.g. in spin-injection experiments). In a paramagnet, the choice of the spin-quantization axis, determined by the direction of the spin polarization, does not influence the band energies, and its most important manifestation is in the changes of the orbital and spin character of the Bloch states. Experimentally, the dependence of the spin relaxation on the SQA was observed in supported graphene layers [27] and in semiconductors [28], where, however, due to the absence of inversion symmetry, the degeneracy between the states (1) and (2) is not present. However, no microscopic theory of anisotropic spin relaxation which explicitly refers to the anisotropy of the Bloch states has been given. In bulk metals with inversion symmetry, which are at the focus of this paper, the Elliott–Yafet mechanism is dominant. In section 3 we will demonstrate that indeed the anisotropy of the EYP in metals can be gigantic.

To our knowledge there is yet no experimental evidence of anisotropy in the spin relaxation of metals, possibly due to the complex setup that would be required for its detection. Ideally one would like to have a single-crystal sample, or at least a sample with a preferential crystallographic orientation. For example, an hcp metal where the c-axis direction is constant throughout the sample should suffice. In addition, one needs a means for creating a spin population with a controlled, varying polarization direction.

As a first example, consider a conduction-electron spin resonance experiment, where the electron levels are split by an externally applied magnetic field, and electrons are resonantly excited between the split levels by microwave radiation [2, 29]. The spin-relaxation time is then inversely proportional to the resonance width. With this setup, the anisotropy would manifest itself as a dependence of the resonance width on the direction of the applied field.

A second example is an experiment of non-local spin detection, as first introduced by Johnson and Silsbee [30]. A ferromagnetic contact is used to inject spin-polarized electrons into a metallic sample. The spins diffuse and are collected at some distance x by a second ferromagnet, whose magnetization is oriented parallel or antiparallel to the first. The difference in chemical potential between the two orientations is read out as a voltage difference $\Delta V(x) \sim \exp(-x/L)$, where L is the spin-relaxation length. If the sample has a preferential crystallographic orientation, one can in principle probe the anisotropy in L by varying the angle between the magnetization direction of the two ferromagnets used for injection with respect to the crystallographic axes in the sample.

1.2. Anomalous Hall effect in ferromagnets

A second phenomenon, for which multiple experimental studies of anisotropy exist [18–25], but no quantitative theoretical argumentation for its emergence had been presented until recently [17], is the anomalous Hall effect [38, 39]. The essence of the AHE in a ferromagnet lies in the generation of a charge current $\mathbf{J}_{\mathrm{H}}$ transverse to the electric field $\mathbf{E}$ (and corresponding 'diagonal' current $\mathbf{J}_0$), without any applied magnetic field [15]. Phenomenologically, the relation between the ith component of the anomalous Hall current and the jth component of the electric field is the following:

$$J_{\mathrm{H},i} = \sigma_{ij}E_j, \tag{5}$$

where σ_{ij} are the components of the anomalous Hall conductivity (AHC) tensor. Since in a ferromagnet the

anomalous Hall conductivity tensor is second rank anti-symmetric, the AHC tensor can be also seen as the AHC vector $\boldsymbol{\sigma}$, whose components are related to the components of the AHC tensor as $\sigma_i = \frac{1}{2}\sum_{jk}\epsilon_{ijk}\sigma_{jk}$, through the Levi-Civita tensor ϵ_{ijk}:

$$\mathbf{J}_{\mathrm{H}} = \mathbf{E} \times \boldsymbol{\sigma}. \tag{6}$$

In general, there can be different contributions to the AHC in a ferromagnet. In a real material, contributions that originate from scattering of electrons off impurities or due to disorder are always present—this is the so-called *extrinsic* AHE [35, 40, 41]. The second important part of the AHE signal—which comes solely from the electronic structure of the pristine crystal—is the so-called *intrinsic* AHE [42]. Namely, the SOC in a perfect crystal gives rise to a transverse spin-dependent *anomalous velocity* of electrons propagating along the direction of the applied electric field—thus leading to the intrinsic anomalous Hall current [4, 43]. In the present work we will focus exclusively on the intrinsic contribution to the AHE.

The intrinsic anomalous Hall conductivity is determined by the electronic structure of the pristine crystal, which can be accurately calculated using modern first-principles methods, see for example a recent review by Gradhand *et al* [44]. Several investigations of intrinsic AHC using first-principles methods have been done, for instance, in $SrRuO_3$ [45, 46], Fe [42, 47], Ni [48], Co [17, 48] and other ferromagnets. For these materials, the calculated intrinsic AHC agrees well with the experimental values, except for the case of fcc Ni [48], which is most probably due to effect of electronic correlations [35, 49]. It is therefore a common belief that the AHE in moderately resistive samples of itinerant ferromagnets is often dominated by the intrinsic contribution.

The intrinsic AHC considered in this work can be obtained via the linear response Kubo formula for the off-diagonal components of the conductivity tensor σ:

$$\begin{aligned} \sigma_{ij} &= -e^2\hbar \int_{\mathrm{BZ}} \frac{\mathrm{d}^3k}{8\pi^3}\, \Omega_{ij}(\mathbf{k}), \\ \Omega_{ij}(\mathbf{k}) &= -2\mathrm{Im} \sum_{n,m}^{o,e} \frac{\langle \psi_{n\mathbf{k}}|v_i|\psi_{m\mathbf{k}}\rangle\langle \psi_{m\mathbf{k}}|v_j|\psi_{n\mathbf{k}}\rangle}{(\varepsilon_{n\mathbf{k}} - \varepsilon_{m\mathbf{k}})^2}, \end{aligned} \tag{7}$$

which relates the conductivity tensor to the Brillouin zone (BZ) integral of the k-dependent Berry curvature tensor Ω. In the latter expression $\psi_{n\mathbf{k}}$ and $\psi_{m\mathbf{k}}$ are respectively the occupied (o) and empty (e) one-electron spinor Bloch eigenstates of the crystal, $\varepsilon_{n\mathbf{k}}$ and $\varepsilon_{m\mathbf{k}}$ are their eigenenergies, and v_i and v_j are the Cartesian components of the velocity operator $\mathbf{v}$. The Berry curvature Ω appearing in the equation above is the very same quantity which arises when the adiabatic dynamics of electrons in the reciprocal space is considered [43]. In particular, the Berry phase acquired by a Bloch electron as it traverses a closed path in the BZ can be calculated as an integral of the Berry curvature over the enclosed area [43, 50]. Mathematically, the Berry curvature is the curvature of the fiber bundle of occupied electronic states in an insulator, and its integral over the whole torus of allowed Bloch vectors provides the value of the quantized transverse charge conductivity, as first demonstrated for the case of the quantum Hall effect by Thouless *et al* [51]. The Berry curvature is also a key quantity in the field of Chern and topological insulators [52, 55]. As suggested by the topological interpretation of the Berry curvature, equation (7) manifests the topological nature of the intrinsic anomalous Hall effect in metals.

Let us briefly outline the concept of anisotropy as it applies to the AHE. The definition is slightly more complicated than for the Elliott–Yafet parameter discussed previously, owing to the vector nature of the anomalous Hall conductivity. The parameter with respect to which the anisotropy of the AHE is studied is the direction of the magnetization $\mathbf{M}$ in the crystal. The anisotropy of the AHC with respect to $\mathbf{M}$ is two-fold: not only the magnitude of $\boldsymbol{\sigma}$ depends on $\mathbf{M}$, but also the direction of $\boldsymbol{\sigma}$ displays a non-trivial dependence on the direction of magnetization. For a high-symmetry direction of $\mathbf{M}$ the AHC vector is aligned with the magnetization so that the Hall current is perpendicular to it. For a general direction of $\mathbf{M}$ away from high-symmetry axes in the crystal the AHC vector can deviate from the direction of $\mathbf{M}$, in which case [17, 20]:

$$\boldsymbol{\sigma}(\mathbf{M}) = \boldsymbol{\sigma}_{\parallel}(\mathbf{M}) + \boldsymbol{\sigma}_{\perp}(\mathbf{M}), \tag{8}$$

where $\boldsymbol{\sigma}_{\parallel}(\mathbf{M})$ is aligned with $\mathbf{M}$ while $\boldsymbol{\sigma}_{\perp}(\mathbf{M})$ is perpendicular to it [17] (see also figure 1). The microscopic origin of the AHE anisotropy is clear from the expression (7) for the Berry curvature, according to which both the dependence of wavefunctions as well as eigenenergies on the magnetization direction leads to the anisotropy of the AHC. It is important to realize that in contrast to the case of paramagnets with inversion symmetry (considered in the following with respect to the anisotropy of the SHE and EYP), for which also the eigenspectrum does not change with the SQA, the dependence of the wavefunctions on the magnetization direction in a ferromagnet is far more complex, owing to broken time-reversal symmetry. Also, the anisotropy of the velocity matrix elements has to be taken into account in uniaxial crystals.

A few remarks are in order concerning the symmetry of the AHC and EYP with respect to the magnetization direction and choice of SQA respectively (both relative to the crystal axes).

The orientation dependence of the AHC tensor $\boldsymbol{\sigma}(\mathbf{M})$ can be described phenomenologically through an expansion in powers of the direction cosines $\{\alpha_i\}$ of $\mathbf{M}$ [53, 54]:

$$\boldsymbol{\sigma}_{ij}(\hat{\mathbf{M}}) = \sum_{p} a_{ijp}\alpha_p + \sum_{pqr} a_{ijpqr}\alpha_p\alpha_q\alpha_r + \cdots, \tag{9}$$

where $\hat{\mathbf{M}}$ is the unit vector along $\mathbf{M}$. Because the AHC is odd under time reversal, $\boldsymbol{\sigma}(-\mathbf{M}) = -\boldsymbol{\sigma}(\mathbf{M})$, only odd powers are present in the above expansion. Crystal symmetry places further constraints on the terms which are allowed in equation (9). In the case of cubic crystals the expansion starts with the third-order term [53]. This is consistent with the small but clearly nonzero anisotropy of the AHC that has been observed in cubic ferromagnets [18–20]. The first-order term in

equation (9) is allowed in uniaxial ferromagnets [53], whose AHC can indeed display a significant anisotropy [17, 21].

A similar expansion can be made for the EYP, with $\hat{\mathbf{M}}$ replaced by the unit vector along the SQA (in a spin resonance experiment, for example, this would correspond to the direction of the magnetic field—see section 3). Since the spin relaxation in a paramagnetic metal is time even (the relaxation time is the same if the initial spin polarization is reversed), only even-order terms are allowed in the expansion in powers of the direction cosines. For cubic crystals the leading angular dependence is of fourth order, while quadratic terms are allowed in uniaxial crystals.

Experimentally, the anisotropy of the anomalous Hall effect in metals is a relatively well-studied phenomenon: see, e.g., experimental data for bcc Fe [18], fcc Ni [19, 20], hcp Gd [21], as well as $FeCr_2S_4$ [22], $Yb_{14}MnSb_{11}$ [23], $Y_2Fe_{17-x}Co_x$ [24] and R_2Fe_{17} (R = Y, Tb, Gd) [25]. For several of the compounds listed above, a strong anisotropy of the transverse current upon changing the direction of the magnetization in the crystal has been observed.

Two basic methods have been used to measure the anisotropy of the AHE. One approach uses a single-crystal sample in the shape of a cylindrical rod of constant diameter. The sample is rotated around its polar axis in a transverse magnetic field, and the Hall voltage is measured as a function of the angle [18]. In the second approach several samples are prepared by cutting plates from coarse monocrystals along specific crystallographic orientations, and the Hall coefficient is then measured for each sample separately [19]. The plates can be cut using, for example, the anode contact method, which allows one to preserve the correct crystallographic structure.

1.3. Spin Hall effect in paramagnets

The spin Hall effect in paramagnets consists in generation of a *spin current* orthogonal to the direction of an applied electric field **E**. In a simple picture, the spin current in the SHE can be seen as two anomalous Hall currents, propagating in opposite directions for spin-up and spin-down electrons. In contrast to the AHE, where the direction of the Hall current is uniquely determined by the directions of **E** and **M**, the spin Hall current propagates in all directions orthogonal to **E**. For each of the directions of the spin current, the 'physical' spin-quantization axis is determined by the direction of the current's spin polarization. First proposed theoretically in 1971 [5], the SHE was re-discovered in 1999 [56], and eventually experimentally observed in 2004 [57], triggering development of new directions in spintronics [58, 59] and further research in the direction of quantum spin Hall insulators [60–63]. In analogy to the anomalous Hall effect, the observed SHE in metals contains two types of contribution: one extrinsic (driven by disorder), and the other intrinsic (disorder independent) [31, 40, 64, 65]. And while very often the spin Hall effect is associated with the resulting spin accumulation at the boundaries of the sample, employing inverse SHE it is possible to measure directly the spin Hall conductivity (SHC), which is much easier to treat theoretically with *ab initio* methods. As in the case of the AHE, for transition metals the experimental SHC values agree very often with the values obtained from first-principles calculations for the intrinsic SHE.

In the first principles calculations presented in section 4 we consider only the intrinsic [31, 60, 64, 66, 67] contribution to the SHC, which results from the virtual interband transitions in the presence of an external electric field. It may be expressed using a linear response Kubo formula analogous to equation (7) for the AHC:

$$\begin{aligned} \sigma_{ij}^{s} &= -e\hbar \int_{\mathrm{BZ}} \frac{\mathrm{d}^3 k}{8\pi^3}\, \Omega_{ij}^{s}(\mathbf{k}), \\ \Omega_{ij}^{s}(\mathbf{k}) &= -2\mathrm{Im} \sum_{n,m}^{o,e} \frac{\langle \psi_{n\mathbf{k}} | Q_i^s | \psi_{m\mathbf{k}} \rangle \langle \psi_{m\mathbf{k}} | v_j | \psi_{n\mathbf{k}} \rangle}{(\varepsilon_{n\mathbf{k}} - \varepsilon_{m\mathbf{k}})^2}, \end{aligned} \tag{10}$$

where Q_i^s is the spatial i- and spin s-component of the spin velocity operator, and the tensor Ω is sometimes referred to as the *spin Berry curvature*. If only the spin-conserving part of the SOC is taken into account, the spin projection along the direction of the spin polarization of the current $\hat{\mathbf{s}}$ is a good quantum number, and the spin velocity operator may be written as $Q_i^s = \frac{\hbar}{2} v_i \tau_s$. In this case the SHC equals twice the value of the (scaled) anomalous Hall conductivity for spin-up electrons only for the same energy bands. Here, τ_s is a Pauli matrix used to express the s-component of the spin operator. In order to treat the spin-non-conserving part of the SOC correctly, we use the definition of the spin current density operator given in [68].

To our knowledge, the only experimental study of anisotropy in the spin Hall effect is the work of Sih *et al* [26] on AlGaAs quantum wells. In metals the anisotropy of the SHE was investigated recently by Freimuth *et al* from first principles [31]. In many aspects, the SHC anisotropy is analogous to that of the anomalous Hall conductivity. It is remarkable, however, that due to the higher symmetry of the problem the anisotropy of the SHC in transition metals is what we call purely *geometrical*. By this term we mean that it is exactly absent in the case of a cubic crystal, while generally the dependence of the magnitude and spin polarization of the spin current on its direction can be reconstructed *exactly* from corresponding values for high-symmetry directions in the crystal. This is in sharp contrast to the behavior of the AHC or EYP, which exhibit anisotropy already in cubic crystals, and for which the dependence of the magnitude of the EYP (or anomalous Hall current) on the direction of the SQA (or the direction of magnetization) cannot be reconstructed from the respective high-symmetry values. Section 4 of this review is dedicated to the anisotropy of the spin Hall effect in transition metals.

Experimentally, two ways can be suggested to study the anisotropy of the SHE. The first method, employed in [26], lies in measuring the spin accumulation (for example via measuring the magneto-optical Kerr rotation) at the sides of the monocrystalline sample, of e.g. cylindrical shape, or even in an in-plane geometry when the sample has the form of a plate or a thin film of a certain crystallographic orientation. Since in a steady current state the spin current propagates in all

directions perpendicular to the electric current, the anisotropy in spin accumulation can be measured under constant electric field in cylindrical samples, while in a two-dimensional geometry the variation in spin accumulation should be probed at one fixed side of the sample while varying the in-plane current direction.

In an alternative approach, the anisotropy of the transverse voltage can be measured and related to the anisotropy of the spin Hall conductivity using the inverse spin Hall effect [69, 70]. In the latter case the spin polarization of the injected spin current can be changed by changing the magnetization direction of the ferromagnet used for spin current injection, which can be achieved by varying the direction of an external magnetic field.

2. Computational methods

For calculations of the Elliott–Yafet parameter and corresponding Fermi surfaces we used density functional theory in the local density approximation [71] to calculate the underlying electronic structure. For the self-consistent calculations we employed the Korringa–Kohn–Rostoker (KKR) Green-function method [72] in the atomic sphere approximation and solve the Dirac equation with angular momentum expansion up to $\ell_{\max} = 4$. The Fermi surface is determined by the KKR secular equation, $\det(\mathcal{M}(\mathbf{k}, E_F)) = 0$, which is equivalent to the condition that at least one eigenvalue of the KKR matrix $\mathcal{M}$ vanishes. We search for the $\mathbf{k}$-vectors fulfilling this condition with a tetrahedron method using linear interpolation of the complex eigenvalues of $\mathcal{M}$. We choose a grid of 200 $\mathbf{k}$-points for each direction in the full BZ, resulting in about 10^7 Fermi-surface points. We followed the procedure described in [73] to maximize the spin component $S_{\mathbf{k}\hat{\mathbf{s}}}$ at the Fermi-surface points. The integration equation (3) is done by evaluating the integrand at the Fermi-surface points and interpolating linearly within the connecting triangles.

For calculations of the intrinsic anomalous Hall and spin Hall conductivities we employed the full-potential linearized augmented plane-wave (FLAPW) method, as implemented in the Jülich code `FLEUR` [74]. We used the generalized gradient approximation to the DFT and experimental lattice constants of the transition metals. The self-consistent calculations with SOC were done in second variation with $k_{\max}$ between 3.7 and 4.0 a.u.$^{-1}$ and about 8000–16 000k-points in the full BZ. For ternary alloys, for instance, $(Fe_{0.5}Co_{0.5})Pt$, the virtual crystal approximation (VCA) was applied on the 3d atomic sites, where the concentration averaged nuclear charge is used instead of that of pure 3d elements and interpolated lattice constants from the neighboring compounds [34] are taken. For the calculations of the conductivities we applied the Wannier interpolation technique of Wang *et al* [47]. We followed the method introduced in [75, 76] to construct the maximally localized Wannier functions (MLWFs) from the FLAPW Bloch states $\psi_{\mathbf{k}m}$:

$$W_{\mathbf{R}n}(\mathbf{r}) = \frac{1}{N}\sum_{\mathbf{k}} \mathrm{e}^{-\mathrm{i}\mathbf{k}\cdot\mathbf{R}} \sum_{m} U^{(\mathbf{k})}_{mn}\psi_{\mathbf{k}m}(\mathbf{r}), \tag{11}$$

where $W_{\mathbf{R}n}$ denotes the nth WF centered at lattice site $\mathbf{R}$, $U^{(\mathbf{k})}_{mn}$ refers to the unitary transformation among the Bloch states at $\mathbf{k}$ which minimizes the spread of the Wannier functions. Using the self-consistent charge density with SOC included, 18 spinor MLWFs per transition metal atom, corresponding to s-, p-, and d-type orbitals, were generated using `wannier90` code [77].

Working in the basis of the maximally localized WFs allows us to construct a real-space tight-binding Hamiltonian of the crystal, which can reproduce the electronic bands with any given accuracy at any k-point in the BZ, given that the necessary number of k-points was used for the generation of the WFs [47]. The real-space tight-binding hopping parameters can be calculated as:

$$H_{mm'}(\mathbf{R}) = \frac{1}{N}\sum_{\mathbf{k}n} \epsilon_{\mathbf{k}n}\mathrm{e}^{-\mathrm{i}\mathbf{k}\cdot\mathbf{R}} \left(U^{(\mathbf{k})}_{nm}\right)^* U^{(\mathbf{k})}_{nm'}, \tag{12}$$

where $H_{mm'}(\mathbf{R})$ denotes the hopping parameter between Wannier orbitals $W_{\mathbf{R}m'}(\mathbf{r})$ and $W_{\mathbf{0}m}(\mathbf{r})$. Based on those parameters, the Hamiltonian, $H(\mathbf{k})$, matrix elements of the velocity operator as well as charge and spin Berry curvature in reciprocal space can be efficiently evaluated using the Wannier interpolation technique [47].

In the section on the anomalous Hall effect, we evaluate the derived perturbation theory expressions for the AHC in $L1_0$ FePt. In order to apply the perturbation theory in the basis of Wannier functions, we use the basis of Wannier functions constructed without SOC to calculate the matrix elements of the spin–orbit interaction. To do this, the scalar-relativistic Hamiltonian without SOC is set up for the majority and minority states, and diagonalized in order to obtain the Bloch functions $\psi^{\sigma}_{\mathbf{k}n}(\mathbf{r})$, with $\sigma = \uparrow$ or $\downarrow$. The matrix elements of SOC in the basis of Bloch states can then be calculated:

$$V^{(\mathbf{k})}_{n\sigma,n'\sigma'} = \sum_{\mu} \frac{\mu_B}{\hbar m_e e c^2} \left\langle \psi^{\sigma}_{\mathbf{k}n} \left| \frac{1}{r}\frac{\mathrm{d}V^{\mu}(r)}{\mathrm{d}r}\mathbf{L}^{\mu}\cdot\mathbf{S} \right| \psi^{\sigma'}_{\mathbf{k}n'} \right\rangle, \tag{13}$$

where $\mathbf{L}^{\mu}$ is the orbital angular momentum operator associated with atom μ (with the potential V^{μ}). In the scalar-relativistic approximation, the spin-dependent Hamiltonian $\tilde{H}^{\sigma}_{mm'}(\mathbf{R})$ can be obtained as:

$$\tilde{H}^{\sigma}_{mm'}(\mathbf{R}) = \frac{1}{N}\sum_{\mathbf{k}n} \epsilon_{\mathbf{k}n\sigma}\mathrm{e}^{-\mathrm{i}\mathbf{k}\cdot\mathbf{R}} \left(U^{(\mathbf{k})}_{nm\sigma}\right)^* U^{(\mathbf{k})}_{nm'\sigma}. \tag{14}$$

Likewise, the matrix elements $V^{(\mathbf{k})}_{n\sigma,n'\sigma'}$ are transformed into the basis set of Wannier functions:

$$V^{\sigma\sigma'}_{mm'}(\mathbf{R}) = \frac{1}{N}\sum_{\mathbf{k}nn'} V^{(\mathbf{k})}_{n\sigma,n'\sigma'}\mathrm{e}^{-\mathrm{i}\mathbf{k}\cdot\mathbf{R}} \left(U^{(\mathbf{k})}_{nm\sigma}\right)^* U^{(\mathbf{k})}_{n'm'\sigma'}. \tag{15}$$

The complete Hamiltonian with SOC in the WF-basis is then given by

$$H^{\sigma\sigma'}_{mm'}(\mathbf{R}) = \tilde{H}^{\sigma}_{mm'}(\mathbf{R})\delta_{\sigma\sigma'} + V^{\sigma\sigma'}_{mm'}(\mathbf{R}). \tag{16}$$

Such a separation enables us to perform the perturbation treatment of SOC. By calculating from first principles an atomic shell averaged SOC parameter $\xi \overset{\text{def}}{=} \langle \frac{1}{r}\frac{\mathrm{d}V(r)}{\mathrm{d}r}\rangle$, it is

possible to write the SOC operator approximately as $\xi \mathbf{L}\cdot\mathbf{S}$, where $\mathbf{L}$ ($\mathbf{S}$) is the total orbital (spin) angular momentum operator. Calculated in such a way the SOC strength ξ for Pt (about 0.6 eV) is one order of magnitude larger than that of 3d elements, for instance, $\xi = 0.06$ eV for Fe.

3. Anisotropy of spin relaxation in metals

First, let us derive the perturbation theory expression for the spin-mixing parameter (see equations (1)–(3)) of a certain state ψ_n (we omit the explicit k-dependence in the following line of arguments). Since we are mainly interested in Fermi-level properties we assume that the eigenenergy of ψ_n coincides with E_F. Let us assume that only the spin-conserving part of the spin–orbit interaction has been included in the Hamiltonian, which has ψ_n as an eigenstate. Since the spin-conserving SOC preserves the spin as a good quantum number, in a paramagnet with structural inversion symmetry the state ψ_n can be characterized by a certain value of spin, e.g., $\psi_n = \psi_n^\uparrow$. This has an exact replica, but of opposite spin $\psi_n^\downarrow$. Upon including into consideration the spin-flip SOC, $\psi_n^\uparrow$ will acquire an admixture of the down spin, which we will denote as $(\psi_n^\uparrow)^\downarrow$, and which corresponds to the part that includes $b_{\mathbf{k}\hat{\mathbf{s}}}$ in equation (1). It is known that the down-spin admixture of $\psi_n^\uparrow$ does not come from interaction with $\psi_n^\downarrow$ at the same energy band, but comes from the interaction with the other states in the system. Within first-order non-degenerate perturbation theory $(\psi_n^\uparrow)^\downarrow$ can be calculated as:

$$(\psi_n^\uparrow)^\downarrow = \xi \sum_{m\neq n} \frac{\langle \psi_m^\uparrow | LS^{\uparrow\downarrow} | \psi_n^\downarrow \rangle}{\varepsilon_n - \varepsilon_m} \psi_m^\downarrow. \tag{17}$$

Since the spin-mixing parameter b_n^2 is equal to $|(\psi_n^\uparrow)^\downarrow|^2$, we readily obtain from the latter expression that

$$b_n^2 \approx \xi^2 \sum_{m\neq n} \frac{|\langle \psi_n^\uparrow | LS^{\uparrow\downarrow} | \psi_m^\downarrow \rangle|^2}{(\varepsilon_n - \varepsilon_m)^2}. \tag{18}$$

Therefore, the spin-mixing parameter of a certain state is just a sum of amplitudes for SOC-mediated spin-flip transitions from this state to other states and back. This picture of the Elliott–Yafet parameter in solids had been suggested by Elliott already in 1954 [1]. Later on in this work, we will apply a similar approach in order to perform a perturbation theory analysis of the Hall effects.

Before proceeding with *ab initio* calculations, we consider a simple model which is able to capture the origin and essential properties of the anisotropy of the spin-mixing parameter in a solid. Namely, let us consider six p-orbitals, p_x^σ, p_y^σ and p_z^σ, with $\sigma = (\uparrow, \downarrow)$ standing for the spin of the orbitals. In order to consider the spin-mixing separately, we explicitly separate the two SOC terms. We have:

$$\begin{aligned} H &= H_0 + \xi (LS)^{\uparrow\uparrow} + \xi (LS)^{\uparrow\downarrow} \\ &= \mathrm{diag}(\varepsilon, \varepsilon+\delta, \varepsilon+\Delta) \otimes 1_{2\times 2} + \xi (LS)^{\uparrow\uparrow} + \xi (LS)^{\uparrow\downarrow}, \end{aligned}$$

where in the on-site part the states p_x^σ and p_y^σ are chosen to be almost degenerate at energy ε (separated by energy $\delta : \delta/\Delta \ll 1$), and the p_z^σ orbitals are shifted to higher energy $\varepsilon + \Delta$ in order to mimic the crystal field splitting by a uniaxial lattice. The SOC strength is given by ξ, with $\xi/\Delta \ll 1$. The energetic levels and their orbital character without spin–orbit coupling are shown in the left column of figure 2, in which δ was set to zero.

Let us first consider the case when the SQA points along the z-axis and $\delta = 0$. When only spin-conserving SOC is added to H_0, the eigenstates are $(\mathrm{p}_x^\sigma \pm \mathrm{i}\mathrm{p}_y^\sigma)/\sqrt{2}$ and p_z^σ ($\sigma = \uparrow, \downarrow$), with energies as sketched in figure 2. The only non-vanishing matrix elements of the spin-flip SOC are $\langle \mathrm{p}_x^\uparrow - \mathrm{i}\mathrm{p}_y^\uparrow | LS^{\uparrow\downarrow} | \mathrm{p}_z^\downarrow \rangle = 2$ and $\langle \mathrm{p}_x^\downarrow + \mathrm{i}\mathrm{p}_y^\downarrow | LS^{\uparrow\downarrow} | \mathrm{p}_z^\uparrow \rangle = -2$ which come from the states that are well separated in energy. According to equations (17) and (18), this leads to a small admixture of the p_z-state of opposite spin in the lowest-lying eigenstate, and corresponding spin-mixing parameter of the order of $(\xi/\Delta)^2$ when the spin-flip SOC is included. On the other hand, when the SQA is chosen along the x-axis, the spin-conserving part of SOC mixes small ξ/Δ-portions of p_y^σ with p_z^σ orbitals, see figure 2. Now, there are four non-vanishing matrix elements of spin-flip SOC, all of order 1, among which two transitions are very close in energy, with a separation of $\sim\xi^2/\Delta$. This results in a very strong spin-mixing between the two low-lying orbitals when the spin-flip SOC is added, with a very large spin-mixing parameter of the lowest-lying state of the order of $(\Delta/\xi)^2$ in first-order perturbation theory, meaning that higher-order perturbation theory is needed, since by definition the spin-mixing parameter cannot exceed $\frac{1}{2}$. The resulting orbital and spin character of the states when the Hamiltonian with complete SOC is diagonalized is presented in the right column of figure 2. Note that the final eigenenergies are the same, irrespective of the SQA, while the character of the states is different among the two directions of the SQA. Obviously, the resulting anisotropy of the spin-mixing parameter of the lowest-lying state with respect to the choice of the SQA is very large if $\xi/\Delta \ll 1$.

The model presented above allows us to make some statements concerning the general conditions under which a large anisotropy of the spin-mixing parameter in a metal can be expected. First of all, crucial is the presence of a degeneracy or near-degeneracy at E_F, of Bloch states originating from the atomic orbitals ϕ_m and $\phi_{m'}$, with the orbital characters $|m - m'| \neq 1$, which are the eigenstates of the $L_{\hat{\mathbf{s}}}$ operator for some direction of the SQA (e.g. z). In this case ($|m - m'| \neq 1$) no direct coupling is allowed between the states by the spin-flip part of the SOC Hamiltonian, and the system is 'protected' against large-amplitude spin-flip transitions, since the spin-mixing occurs due to interaction with other, energetically different, states. Correspondingly, the further away these other states are from the Fermi energy, the smaller the spin-mixing parameter will be. This is exemplified for our model in figure 3 (right), where for the splitting $\delta = 0$ between the p_x and p_y orbitals we observe a decay of the spin-mixing parameter of the lowest-lying state with increasing separation Δ with the higher lying p_z orbital for the SQA along z. In this case, for a considerably large Δ, also the relative position of the states ϕ_m and $\phi_{m'}$ with respect to each other is not that important for the spin-mixing parameter,

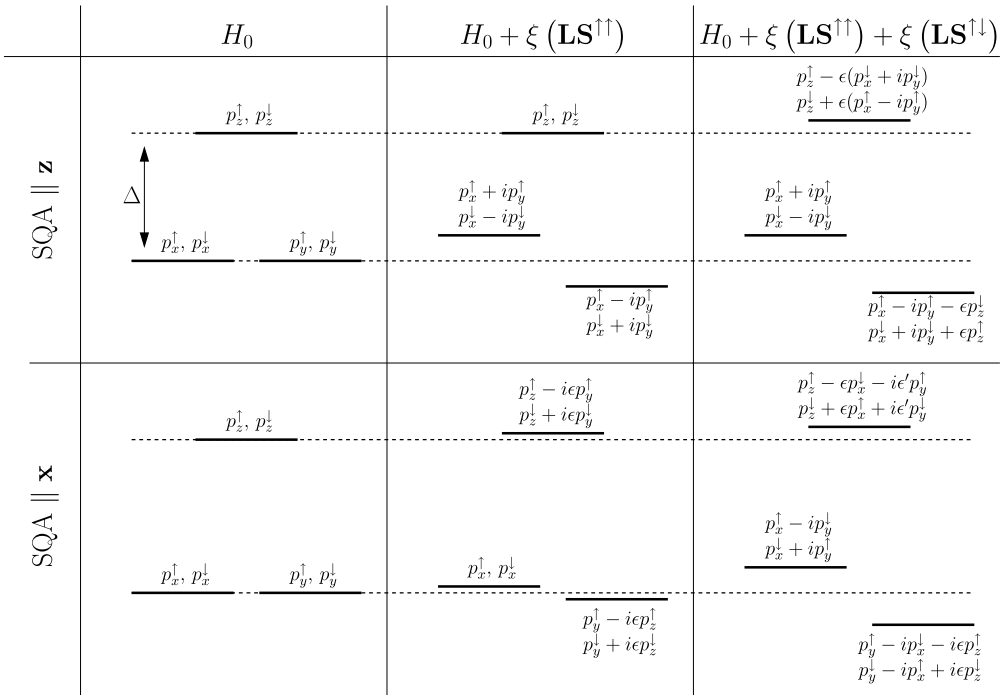

Figure 2. Eigenvalues of the spin-degenerate p-states described by the Hamiltonian $\mathrm{diag}(\varepsilon, \varepsilon, \varepsilon + \Delta) \otimes \mathbb{1}_{2\times2}$ ($\mathbb{1}_{2\times2}$ is the unit matrix in spin space) (left column), including the spin-conserving part of SOC for two different quantization axes (middle column), and including both spin-conserving and spin-flip parts of SOC for two different quantization axes (right column). For each doubly degenerate state the orbital and spin decomposition is annotated. Note that while the energy spectrum is identical for both SQA's in the right column, the spin character of the two low-lying states is different, which gives rise to the anisotropy of the spin-mixing parameter. In the labels, 'ϵ' and 'ϵ'' denote a small admixture of the corresponding state of the order of ξ/Δ.

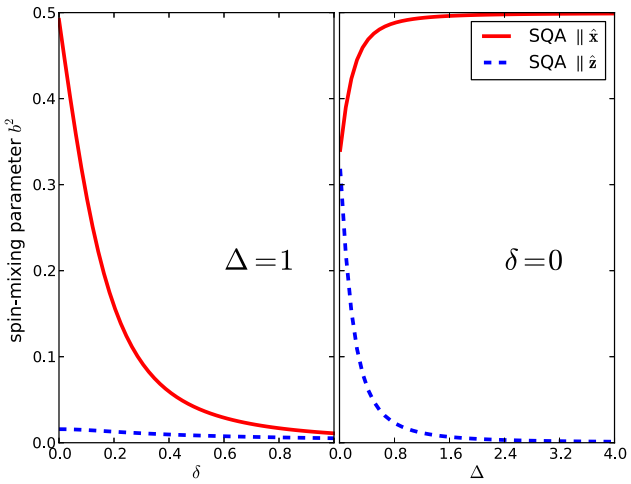

Figure 3. Dependence of the spin-mixing parameter of the lowest-lying state in the model from figure 2 on the separation δ between nearly degenerate p_x and p_y states at constant separation with the p_z orbital $\Delta = 1$ (left), and on the separation Δ of degenerate p_x and p_y states ($\delta = 0$) with the p_z orbital (right). The SOC strength of 0.1 eV was taken for these calculations. Clearly, the largest anisotropy of the spin-mixing parameter is acquired when the states p_x and p_y are perfectly degenerate and are lying far away from the p_z orbital.

as is clear from figure 3 (left), in which at constant Δ of 1 eV the parameter δ is varied, and the observed variation of the spin-mixing parameter of the lowest-lying state is small if $\delta \ll \Delta$.

On the other hand, for the SQA along the x-axis, the spin-mixing between the nearly degenerate states ϕ_m and $\phi_{m'}$ is favored and reaches very large values, since the matrix elements of the spin-flip SOC between these orbitals are non-vanishing. As can be seen in figure 3, the spin-mixing parameter is largest for small values of δ and rapidly decreases as the separation between initially degenerate states is increased. The fraction of spin-mixing of the nearly degenerate states that arises from interaction with other states is minimal, but it reduces the overall value of the spin-mixing parameter. The suppression of the spin-mixing parameter of the states at the Fermi energy due to interaction with the higher-lying states is reduced, the further the latter are from the Fermi energy, as clearly visible in figure 3, in which Δ is varied at constant $\delta = 0$. Overall, by examining figure 3, we conclude that the largest anisotropy of the spin-mixing parameter will be favored when the states with $|m - m'| \neq 1$ at the Fermi level are perfectly degenerate, and are positioned very far away from other states. To summarize the central argument: the spin-flip part of SOC depends on the choice of the SQA. If the SQA is along z, then the spin-flip SOC does not couple states with $|m - m'| \neq 1$; if the SQA is along x or y, then it does couple them.

Let us now turn to realistic material calculations from first principles. We begin with hcp osmium, which we choose as an example of a typical transition metal with a uniaxial crystal structure. First, we take a look at the band structure of Os along the Γ–A path from the BZ center along the z-axis to the center of the hexagonal BZ face, presented in

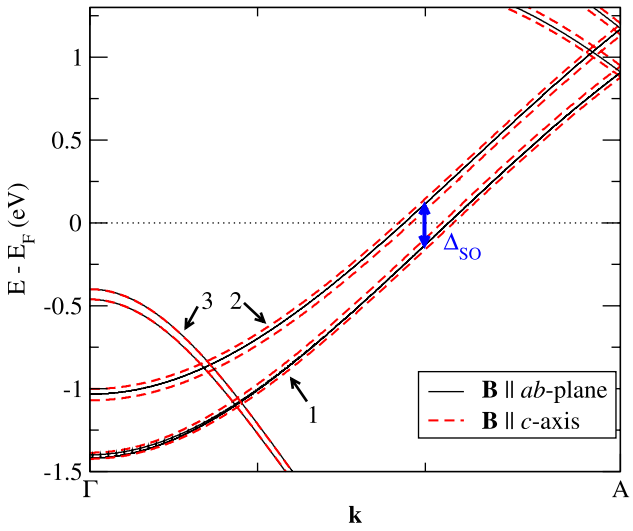

Figure 4. Band structure of hcp osmium around the Fermi level, in the direction Γ–A (BZ center to center of hexagonal face) with applied **B**-field of 40 meV. The exchange splitting of the two bands crossing the Fermi energy (1 and 2) depends on the direction of **B**, reflecting the anisotropy of the spin-mixing at the hot spot 'H' in figure 5.

figure 4. The splitting of the two bands (each band is doubly degenerate) which cross the Fermi level here ('1' and '2', full lines) is due to the spin–orbit interaction, as can be verified from the fact that they fall on top of each other when scaling down the spin–orbit coupling strength. Also, without SOC, it is straightforward to determine the orbital character of the bands: in this case the bands have a d_{+1} and d_{-1} character, which are superimposed to form the d_{xz} and d_{yz} states. Overall, we have all the prerequisites for a large anisotropy of the Elliott–Yafet parameter at this point of the Fermi surface, according to the arguments presented above, since bands '1' and '2' are well separated from other bands at the crossing with the Fermi level and the associated orbitals have $|m - m'| = 2$. Before proceeding with an explicit calculation of the Elliott–Yafet parameter we perform a numerical experiment in order to examine the anisotropy of the response of the bands in figure 4 to a small Zeeman-like field **B** with a magnitude of 40 meV. The small Zeeman field, which we apply by hand, lifts the remanent degeneracy owing to the coupling to the Bloch states of the form $\mathbf{B}\cdot\boldsymbol{\tau}$, which breaks the time-reversal symmetry and defines a spin-quantization axis in the direction of **B**. In figure 4 we clearly observe a splitting of bands '1' and '2' for **B** along the *c*-axis in the crystal (dashed lines). However, for **B** in the *ab*-plane, the degenerate pairs '1' and '2' do not split (solid lines), which marks a very anisotropic response to a Zeeman magnetic field.

The calculated Fermi surface of Os presented in figures 5(a)–(c) consists of two nested sheets, a surrounding surface crossing the BZ boundary and little hole pockets (denoted by '*P*'). The latter ones are ellipsoids in an extended zone scheme, centered around a point on the BZ boundary. Analyzing the distribution of the spin-mixing parameter $b^2_{\mathbf{k}\hat{\mathbf{s}}}$ on the Fermi surface, we observe a strong dependence on the SQA, evident from comparing figures 5(a) and (b). For $\hat{\mathbf{s}}$ along the *c*-axis of the crystal, figure 5(a), the spin-mixing is relatively uniform ($b^2_{\mathbf{k}\hat{\mathbf{s}}} \approx 0.05$) for large areas of the Fermi surface, reaching higher values near the pockets. However, this picture changes drastically when $\hat{\mathbf{s}}$ is in the *ab*-plane (figure 5(b)). In this case, the areas with full spin-mixing (red, $b^2_{\mathbf{k}\hat{\mathbf{s}}} \approx 0.5$) are prominent, most clearly at the caps of the two nested Fermi-surface sheets, indicated by 'H', which

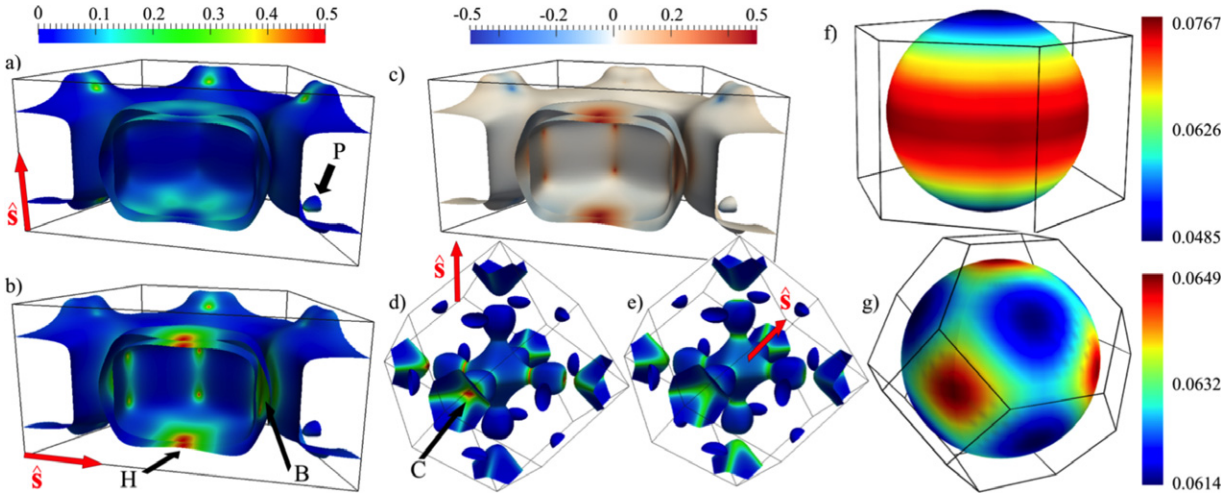

Figure 5. Fermi surfaces of Os ((a)–(c)) and W ((d)–(e)). For an illustration of the nested sheets only half of the Fermi surface of Os is shown. The Elliott–Yafet parameter $b^2_{\mathbf{k}\hat{\mathbf{s}}}$ is shown with a color code on the Fermi surface with the SQA along the *c*-axis (a) and in the *ab*-plane (b). Red arrows at the left-lower corner of (a) and (b) indicate the direction of the SQA. The difference of $b^2_{\mathbf{k}\hat{\mathbf{s}}}$ between the two directions of $\hat{\mathbf{s}}$ is shown in (c). Analogously, $b^2_{\mathbf{k}\hat{\mathbf{s}}}$ for $\hat{\mathbf{s}}$ along [001] and [111] in W is shown in (d) and (e), respectively. The averaged values of $b^2_{\hat{\mathbf{s}}}$ over all directions of $\hat{\mathbf{s}}$, corresponding to polycrystalline samples, are 0.0666 for Os and 0.0627 for W. Note that the color scale above (a) refers to ((a), (b), (d), (e)) while the color scale above (c) refers only to (c). In (f) and (g), the integrated Elliott–Yafet parameter $b^2_{\hat{\mathbf{s}}}$ is shown as function of the SQA direction for Os and W, respectively (different color scale). Partly adapted from [36].

are formed by bands 1 and 2 crossing the Fermi level in figure 4. Additionally, large areas with smaller, but still strong spin-mixing ($b^2_{\mathbf{k}\hat{\mathbf{s}}} \approx 0.3$), are visible, e.g. in the region denoted by 'B'. Overall, for the two considered cases there is a strong qualitative difference in the **k**-dependent spin-mixing parameter $b^2_{\mathbf{k}\hat{\mathbf{s}}}$. We can understand now the anisotropy of the response to the magnetic field in figure 4: employing the perturbation theory arguments, the energy splitting of a state due to the presence of a small Zeeman field is proportional to $b^2_{\mathbf{k}\hat{\mathbf{s}}}$, which is strongly anisotropic in the vicinity of the 'H'-point.

As for the Fermi-surface averaged values $b^2_{\hat{\mathbf{s}}}$, we find $b^2_{\hat{\mathbf{s}}}$ of 4.85×10^{-2} and 7.69×10^{-2} for $\hat{\mathbf{s}}$ along the *c*-axis and the *ab*-plane, respectively, yielding thus a gigantic anisotropy of the Elliott–Yafet parameter, defined as $\mathcal{A} = \left[\max_{\hat{\mathbf{s}}}(b^2_{\hat{\mathbf{s}}}) - \min_{\hat{\mathbf{s}}}(b^2_{\hat{\mathbf{s}}})\right] / \min_{\hat{\mathbf{s}}}(b^2_{\hat{\mathbf{s}}})$, of 59%. On the other hand, the anisotropy with respect to rotations of the SQA within the *ab*-plane is negligible. These two limiting cases are contained in figure 5(f), in which the value of $b^2_{\hat{\mathbf{s}}}$ is shown as a function of $\hat{\mathbf{s}}$ for all possible directions of $\hat{\mathbf{s}}$. The absent (or very small) anisotropy in the *ab*-plane is reflected in the rotationally invariant color scale around the *c*-axis, as opposed to the large difference between the *ab*-plane and the *c*-axis. The difference of $b^2_{\mathbf{k}}$ for the two limiting cases of SQA for each point at the Fermi surface is shown in figure 5(c). Large areas of the Fermi surface show a small orientational dependence of $b^2_{\mathbf{k}}$ (white areas). The anisotropy at the hot spots is very large, but the sign is different between the hot spot 'H' and the hot spots near the pockets. The magnitude of the effect is strongly enhanced by the large extension of the two near-degenerate, parallel sheets of the Fermi surface, resulting in a spin-flip 'hot area' around *H* instead of a single 'hot spot'. In addition, the reduced symmetry helps: if the crystal had cubic symmetry, then upon a change of the SQA from *z* to *x* the effects at rotationally equivalent parts of the Fermi surface would mutually cancel.

The mechanism for large anisotropy of the spin-mixing parameter described above is of course not only specific to the d-states of Os, but it is also responsible for the large values of $\mathcal{A}$ that we find for hcp Lu (200%), hcp Re (88%) and hcp Hf (830%). Particularly in hcp metals there is a special symmetry at the hexagonal face of the Brillouin zone that is lifted only by the SOC. Thus, whenever the Fermi surface of an hcp metal happens to cut through the hexagonal face, the resulting contour can obtain full spin-mixing depending on the SQA, as shown in [36] for Hf. These loop-like contours, or spin-flip hot loops, are a source of extremely high anisotropy. The Fermi surfaces of Lu, Re and Hf, for example, contain such loops, but the one of Os does not, since it does not cut through the hexagonal face.

Next, we analyze the hot-spot contribution to the averaged $b^2_{\hat{\mathbf{s}}}$ and the anisotropy $\mathcal{A}$. We perform integrals similar to Eq. (3), but restricting the integration to the part of the Fermi surface where $b^2_{\mathbf{k}\hat{\mathbf{s}}}$ lies in certain intervals, $x_i < b^2_{\mathbf{k}\hat{\mathbf{s}}} \leq x_{i+1}$, with $x_i = 0, 0.05, 0.10, \ldots$. This integration results in values $\tilde{b}^2_{\hat{\mathbf{s}}}$ which form the histogram presented in figure 6. As we can see, for the SQA along the *c*-axis, $b^2_{\hat{\mathbf{s}}}$ is

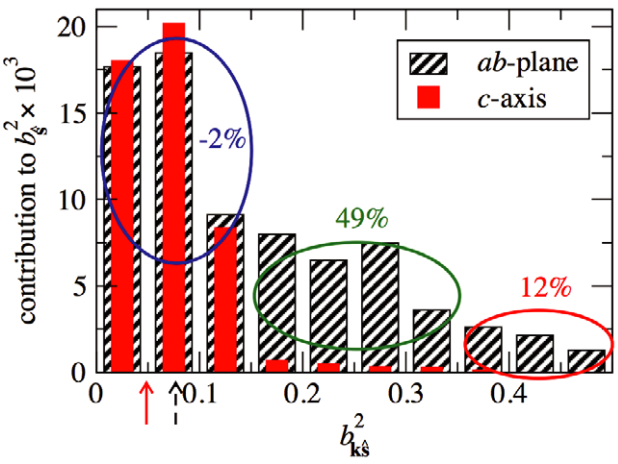

Figure 6. Contribution to the Os Fermi-surface average, $b^2_{\hat{\mathbf{s}}}$, as a function of $b^2_{\mathbf{k}\hat{\mathbf{s}}}$. The solid (dashed) arrow denotes $b^2_{\hat{\mathbf{s}}}$ for the SQA along the *c*-axis (in the *ab*-plane). The values correspond to the respective contribution of each region to the partial anisotropy $\tilde{\mathcal{A}}$, leading to a total anisotropy $\mathcal{A}$ of 59%. Note that while the anisotropy of the EYP is clearly dominated by the intermediate region of $b^2_{\mathbf{k}\hat{\mathbf{s}}}$, the major contribution to the EYP for both directions of the SQA comes from the region with $b^2_{\mathbf{k}\hat{\mathbf{s}}} < 0.15$ (96% and 60% for the SQA along the *c*-axis and in the *ab*-plane, respectively).

mainly determined by regions with not so high spin-mixing parameter ($b^2_{\mathbf{k}\hat{\mathbf{s}}} < 0.15$), leading to the total value of 4.85×10^{-2} (denoted by the solid arrow). For $\hat{\mathbf{s}}$ in the *ab*-plane there is also a considerable contribution from regions with $b^2_{\mathbf{k}\hat{\mathbf{s}}} > 0.15$, increasing the total value to 7.69×10^{-2} (dashed arrow). Comparing the two histograms for different SQA, we can draw conclusions about the partial contribution of each region to the anisotropy, $\tilde{\mathcal{A}} = (\tilde{b}^2_{ab} - \tilde{b}^2_{c})/b^2_{c}$. Interestingly, the anisotropy originates not only from the hot spots with $b^2_{\mathbf{k}\hat{\mathbf{s}}} > 0.35$, leading to $\tilde{\mathcal{A}} = 12\%$, but to a large extent from the areas with intermediate spin-mixing $0.15 < b^2_{\mathbf{k}\hat{\mathbf{s}}} \leq 0.35$ around the hot spots and regions 'B', resulting in $\tilde{\mathcal{A}} = 49\%$. The larger area with low spin-mixing, $b^2_{\mathbf{k}\hat{\mathbf{s}}} \leq 0.15$, does not contribute to the anisotropy significantly ($\tilde{\mathcal{A}} = -2\%$).

Let us now turn to tungsten, which has a bcc lattice structure, and see whether higher symmetry of the lattice brings qualitative changes in the anisotropy of the EYP. When $\hat{\mathbf{s}} \parallel [001]$, $b^2_{\mathbf{k}\hat{\mathbf{s}}}$ exhibits hot spots in directions perpendicular to $\hat{\mathbf{s}}$ (denoted by 'C' in figure 5(d)), following a formation scenario similar to that at the 'H'-point in Os. Additionally, many states with smaller spin-mixing ($0.2 < b^2_{\mathbf{k}\hat{\mathbf{s}}} < 0.3$) are present at the Fermi surface, leading to $b^2_{\hat{\mathbf{s}}} = 6.49 \times 10^{-2}$. For the SQA along another high-symmetry direction of the lattice, $\hat{\mathbf{s}} \parallel [111]$ in figure 5(e), the intensity at the point 'C' is reduced, but a large area with smaller spin-mixing is clearly present, resulting in $b^2_{\hat{\mathbf{s}}} = 6.14 \times 10^{-2}$. For SQA along [110], we find $b^2_{\hat{\mathbf{s}}} = 6.26 \times 10^{-2}$. This leads to an anisotropy $\mathcal{A} = 6\%$, which is still large but one order of magnitude smaller than in hcp Os. This observation is similar to the dependence of the magneto-crystalline anisotropy energy [78] and anisotropy of the intrinsic anomalous Hall conductivity [17] on the symmetry of the lattice in

ferromagnetic crystals: the cubic W crystal exhibits a fourfold rotational axis, causing SOC to contribute to $\mathcal{A}$ in the fourth order. In the uniaxial hcp structure, an axis perpendicular to the c-axis is only two-fold, and SOC enters $\mathcal{A}$ already in the second order. Nevertheless, the comparatively large anisotropy of spin relaxation in W is partly a consequence of the d-states, which yield a strong directional anisotropy of the Fermi surface. In contrast to this, the Fermi surface of gold, for example, consists of s-like states and can be regarded as almost spherical. For the Elliott–Yafet parameter in Au, we find a value of $b^2_{\hat{\mathbf{s}}} \approx 3.25 \times 10^{-2}$, which is comparable in magnitude to that in W and Os, but the anisotropy is one order of magnitude smaller than in W. Looking at the symmetry of $b^2_{\mathbf{k}\hat{\mathbf{s}}}$ in W, we recognize that it is lower than the symmetry of the lattice. And although for a spin-quantization axis along [001] the fourfold rotational symmetry of the lattice around this axis is retained by $b^2_{\mathbf{k}\hat{\mathbf{s}}}$, figure 5(d), further symmetry breaking will occur for an arbitrary direction of the SQA, leaving only those point-group symmetry operations of the lattice that map the SQA to itself, plus the inversion symmetry $\mathbf{k} \to -\mathbf{k}$. In contrast, for the integrated value $b^2_{\hat{\mathbf{s}}}$ the full symmetry of the lattice is obviously retained.

To conclude, we underline that the spin relaxation in metals can strongly depend on the orientation of the spin polarization of injected electrons due to a corresponding anisotropy of the Elliott–Yafet coefficient [36]. The anisotropy is expected to be largest in non-cubic crystals, in the presence of extended, nested Fermi-surface sheets that are almost degenerate, resulting in delocalized spin-flip hot areas instead of singular spin-flip hot spots. Especially critical are cases where the splitting is caused primarily by the spin–orbit coupling. Since there is no theoretical limit on the area of the nested sheets in this scenario, the anisotropy of the EYP can be in principle *colossal*, exceeding the values calculated and presented here for W, Os, or even Hf.

4. Anisotropy of intrinsic spin Hall effect in metals

The spin current is characterized by the velocity and the spin polarization. Hence, the spin current density $\mathbf{Q}$ is a tensor in $\mathbb{R}^3 \otimes \mathbb{R}^3$ spanned by the basis vectors $\hat{\mathbf{e}}_i \otimes \hat{\mathbf{f}}_k$. For clarity we use the symbols $\hat{\mathbf{f}}_x$, $\hat{\mathbf{f}}_y$ and $\hat{\mathbf{f}}_z$ to denote the unit vectors of spin polarization, while $\hat{\mathbf{e}}_x$, $\hat{\mathbf{e}}_y$ and $\hat{\mathbf{e}}_z$ are the unit vectors of velocity. In terms of the spin Hall conductivity tensor, σ^k_{ij} (which has three indices: i denotes the direction of spin current, j the direction of applied external electric field, and k the direction of spin polarization of the spin current), the spin current density for a general direction of electric field is given by

$$\mathbf{Q} = \sum_{ijk} \sigma^k_{ij} \hat{\mathbf{e}}_i \otimes \hat{\mathbf{f}}_k E_j. \tag{19}$$

While the anisotropy of the AHE manifests itself in the dependency of the magnitude of the conductivity vector on the magnetization direction, in the case of the SHE in paramagnets there is no magnetization vector $\mathbf{M}$ to control, only the direction of the applied electric field can be varied. However, the spin polarization of the induced spin current depends on the direction in which the spin current is measured (see figure 7(a)).

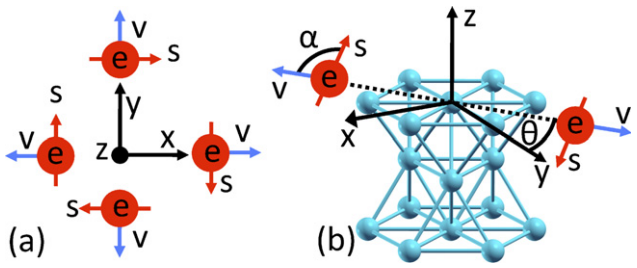

Figure 7. (a) Spin currents in cubic systems induced by an electric field along the z-axis. The spin $\mathbf{s}$ points always perpendicular to the velocity $\mathbf{v}$. (b) Hexagonal hcp structure of the transition metal Ti. The spin current in direction $\hat{\mathbf{n}} = (0, \cos\theta, \sin\theta)^{\mathrm{T}}$ induced by an electric field in the x-direction is not perpendicular to the velocity $\mathbf{v}$ for a general angle θ, i.e., $\mathbf{v}$ and $\mathbf{s}$ enclose an angle $\alpha \neq 90°$. Reprinted with permission from [31]. Copyright 2010 by the American Physical Society.

Hence, for a fixed electric field a given spin polarization $\hat{\mathbf{s}}$ propagates in its 'own' direction, specified by σ^k_{ij}. This direction is given by the vector $\mathbf{Q}^{\hat{\mathbf{s}}} = \mathbf{Q} \cdot \hat{\mathbf{s}}$, where the dot product implies contraction with the vectors $\hat{\mathbf{f}}_k$ of equation (19). If, in analogy with equation (6), we define a spin Hall conductivity vector $\boldsymbol{\sigma}(\hat{\mathbf{s}})$ as

$$\sigma_l(\hat{\mathbf{s}}) = \tfrac{1}{2} \sum_{ijk} \epsilon_{ijl} \sigma^k_{ij} s_k, \tag{20}$$

then $\mathbf{Q}^{\hat{\mathbf{s}}}$, which is the spin current density for polarization along $\hat{\mathbf{s}}$, obeys (according to equation (19)) the relation

$$\mathbf{Q}^{\hat{\mathbf{s}}} = \mathbf{E} \times \boldsymbol{\sigma}(\hat{\mathbf{s}}). \tag{21}$$

The direction of $\boldsymbol{\sigma}(\hat{\mathbf{s}})$ always depends on $\hat{\mathbf{s}}$, but the magnitude not necessarily so. We call the *SHE in a material anisotropic*, if the magnitude of $|\boldsymbol{\sigma}(\hat{\mathbf{s}})|$ depends on $\hat{\mathbf{s}}$.

In cubic systems symmetry requires that $\sigma^k_{ij} = \sigma^z_{xy} \epsilon_{ijk}$. Thus, the SHC may be expressed in terms of one material parameter, equation (21) simplifies to $\mathbf{Q}^{\hat{\mathbf{s}}} = \sigma^z_{xy} \mathbf{E} \times \hat{\mathbf{s}}$, and the conductivity vector is $\boldsymbol{\sigma}(\hat{\mathbf{s}}) = \sigma^z_{xy} \hat{\mathbf{s}}$. Since the magnitude of the conductivity vector, σ^z_{xy}, is independent of $\hat{\mathbf{s}}$, the SHE is isotropic in cubic systems. The relationship between the direction of spin current and the direction of spin polarization in cubic systems is illustrated in figure 7(a). For the spin-mixing parameter and the anomalous Hall effect the dependence on the direction of the SQA and magnetization in the sample, respectively, can be more complicated even in cubic crystals, see e.g. figures 5(d)–(e).

Let us consider now rigorously the situation of the SHE in transition metals with hcp structure, figure 7(b), keeping in mind that the following results remain valid also for general uniaxial structures. If the electric field is applied along the x-direction, the magnitude of the spin current in the y-direction will generally differ from that in the z-direction since the x-axis exhibits only two-fold rotational symmetry. The spin current density in direction $\hat{\mathbf{n}} = (0, \cos\theta, \sin\theta)^{\mathrm{T}}$ is

$$\hat{\mathbf{n}} \cdot \mathbf{Q} = -(\sigma^z_{xy} \hat{\mathbf{f}}_z \cos\theta - \sigma^y_{zx} \hat{\mathbf{f}}_y \sin\theta) E_x. \tag{22}$$

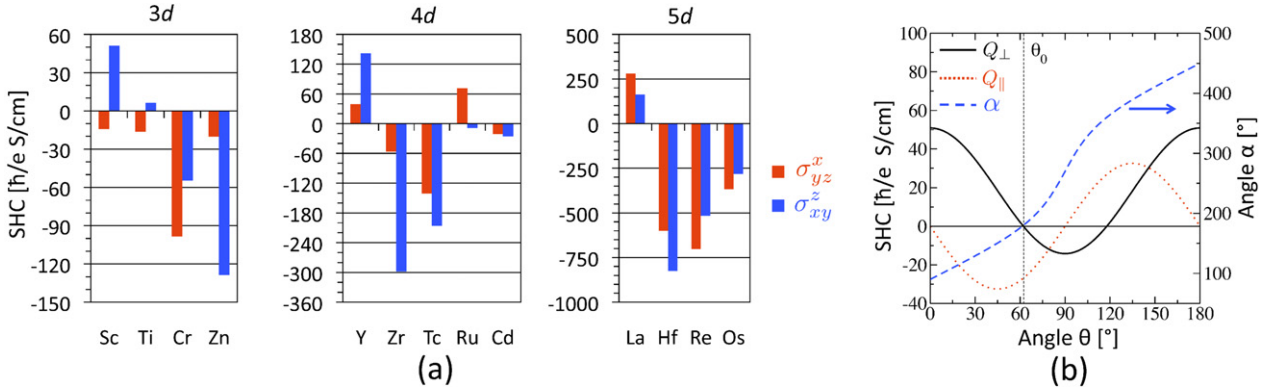

Figure 8. (a) For the hcp metals Sc, Ti, Zn, Y, Zr, Tc, Ru, Cd, La, Hf, Re and Os and for antiferromagnetic Cr the spin Hall conductivities σ^x_{yz} and σ^z_{xy} are shown as light (red) and dark (blue) bars, respectively. (b) Decomposition of the SHC of Sc into perpendicular and parallel components following equation (23). The angle α enclosed by the direction of the spin current and the direction of the spin polarization is also shown. At the angle $\theta_0 = 62.2°$ the component of the spin polarization perpendicular to the spin current vanishes and $\alpha = 180°$. Reprinted with permission from [31]. Copyright 2010 by the American Physical Society.

Note that according to equation (19) $\hat{\mathbf{n}} \cdot \mathbf{Q}$ is a vector pointing in the direction of spin polarization. We define the anisotropy of the SHE for spin polarization in the yz-plane as $\Delta_{zy} = \sigma^z_{xy} - \sigma^y_{zx}$. Physically, if σ^z_{xy} and σ^x_{yz} have the same sign, parameter Δ_{zy} quantifies the difference in the magnitude of the spin current measured along the y and z axes, when the electric field points along x. For a general angle θ the components of the spin current with spin polarization parallel to $\hat{\mathbf{n}}$ ($Q_\parallel$) and spin polarization perpendicular to $\hat{\mathbf{n}}$ ($Q_\perp$) are given by

$$\begin{aligned} Q_\parallel &= \hat{\mathbf{n}} \cdot \mathbf{Q} \cdot \hat{\mathbf{n}} = -\tfrac{1}{2}\Delta_{zy} \sin(2\theta) E_x, \\ Q_\perp &= (\sigma^y_{zx} + \Delta_{zy} \cos^2\theta) E_x. \end{aligned} \tag{23}$$

If $\Delta_{zy} \neq 0$, the spin polarization is perpendicular to $\hat{\mathbf{n}}$ only if $\hat{\mathbf{n}}$ is along the y- or z-direction, otherwise the spin polarization and direction of spin current enclose the angle $\alpha = \arctan(Q_\perp/Q_\parallel) \neq 90°$, as shown in figure 7(b). It follows from equation (23) that $Q_\perp$ is zero at the angle

$$\theta_0 = \arccos \sqrt{-\sigma^y_{zx}/\Delta_{zy}} \tag{24}$$

if σ^z_{xy} and σ^y_{zx} differ in sign. At this angle θ_0 the spin polarization and the spin current are collinear. This is an interesting constellation, which cannot occur in cubic systems. An analogous situation can also occur for the anomalous Hall effect, i.e. a different sign of the AHC for two different high-symmetry directions of the magnetization in the crystal, as we show in section 5.1. In the latter case, there exists a direction of the magnetization in the crystal for which the Hall current (spin current in SHE) and the magnetization (spin polarization in SHE) are collinear. Motivated by the rotational sense of the Hall current as the magnetization direction is rotated, we call this effect the *anti-ordinary Hall effect*, see section 5.1.

The case of spin current in the x-direction and electric field $\mathbf{E} = (0, E\cos\theta, E\sin\theta)^{\mathrm{T}}$ in the yz-plane is simply related to the previous one by a minus sign: the components of the spin current with spin polarization parallel and perpendicular to the electric field $\mathbf{E}$ are given by $Q_\parallel = \frac{1}{2}\Delta_{zy} \sin(2\theta)E$ and $Q_\perp = -(\sigma^y_{zx} + \Delta_{zy}\cos^2\theta)E_x$, respectively. At the angle θ_0, equation (24), the spin polarization and the electric field are collinear. Thus, one can achieve collinearity of the spin polarization and electric field, or collinearity of the spin polarization and direction of spin current if σ^z_{xy} and σ^y_{zx} differ in sign. For the anti-ordinary anomalous Hall effect this means that we can find a direction of $\mathbf{E}$ such that the Hall current is collinear to the magnetization, while the transverse Hall current is not zero.

If the electric field is applied along the z-axis, the same magnitude of the spin current will be measured in all directions perpendicular to the z-axis, since the z-axis exhibits three-fold rotational symmetry. The spin current in direction $\hat{\mathbf{n}} = (\cos\theta, \sin\theta, 0)^{\mathrm{T}}$ is in this case

$$\hat{\mathbf{n}} \cdot \mathbf{Q} = (\sigma^x_{yz} \hat{\mathbf{f}}_x \sin\theta - \sigma^y_{zx} \hat{\mathbf{f}}_y \cos\theta) E_z. \tag{25}$$

Symmetry requires that $\sigma^y_{zx} = \sigma^x_{yz}$. Consequently, the magnitude of the spin current is independent of θ and the spin polarization is perpendicular to both the electric field and $\hat{\mathbf{n}}$.

In the case of the hcp structure the conductivity vector and the spin current density, equation (21), may be expressed in terms of the anisotropy as

$$\begin{aligned} \boldsymbol{\sigma}(\hat{\mathbf{s}}) &= \sigma^x_{yz} \hat{\mathbf{s}} + (0, 0, \Delta_{zy} s_z)^{\mathrm{T}}, \\ \mathbf{Q}^{\hat{\mathbf{s}}} &= \sigma^x_{yz} \mathbf{E} \times \hat{\mathbf{s}} + \Delta_{zy} s_z (E_y, -E_x, 0)^{\mathrm{T}}. \end{aligned} \tag{26}$$

Hence, only two parameters, σ^x_{yz} and Δ_{zy}, suffice to describe the SHE in hcp nonmagnetic metals. The fact that one needs only two parameters to reconstruct the exact analytical dependence of the spin polarization on the direction in which the spin current is measured is a manifestation of the *geometrical anisotropy* of the SHE. This is a major difference from the anomalous Hall effect and spin relaxation, for which the conductivity vector and the EYP have to be recalculated anew for each direction of the magnetization and SQA, since the EYP and the AHC for a general direction of the SQA/magnetization cannot be related to the corresponding values for the high-symmetry axes. For example, in the case of the AHE, already four parameters are needed for an

approximate expansion of the conductivity of hcp crystal up to third order in the directional cosines [17].

Next, we present in figure 8 the results of first-principles calculations of the intrinsic SHC, equation (10), for the hcp metals Sc, Ti, Zn, Y, Zr, Tc, Ru, Cd, La, Hf, Re, Os and for antiferromagnetic Cr (see section 2 for computational details). In the case of Cr we neglected the spin density wave and considered the antiferromagnetic structure with two atoms in the unit cell and with the magnetic moments parallel and antiparallel to the z-axis. Except for Cd, all metals studied in this work exhibit a large anisotropy of SHE, which we expect to be clearly visible in experiments. Of particular interest are the hcp metals Sc, Ti and Ru, where the sign of the conductivity changes as the spin polarization is rotated from the z-axis into the xy-plane. As discussed before, collinearity of the spin polarization and the electric field or the spin polarization and the spin current may be achieved if the electric field (the spin current) lies in the yz-plane at the angle θ_0, equation (24), from the y-axis. To illustrate this we plot in figure 8(b) the angle α enclosed by the direction of the spin current and the direction of the spin polarization as well as the SHCs associated with $Q_{\parallel}$ and $Q_{\perp}$ (see equation (23)) as a function of the angle θ for Sc. The critical angles at which the perpendicular component of the spin polarization vanishes are $\theta_0 = 62.2°$, $\theta_0 = 32.1°$, and $\theta_0 = 19.1°$ for Sc, Ti, and Ru, respectively. Note that in case of Ru we have the case of a *colossal anisotropy* of the SHE: the values of the two calculated conductivities differ by an order of magnitude. In the case of Cr the SHE is anisotropic, as the cubic symmetry is broken by the staggered magnetization: if the spin polarization of the spin current is perpendicular to the staggered magnetization then the SHC is larger by a factor of 1.8 compared to the case of spin polarization parallel to the staggered magnetization. We can thus claim that in antiferromagnets the direction of the local spins presents an additional channel for the SHE anisotropy. Such anisotropy is no longer geometrical, however, due to the dependence of the electronic structure on the direction of local magnetization, similarly to the case of the AHE in ferromagnets.

Generally, a simple analysis of the SHC and its anisotropy in terms of a simple model becomes very difficult, since (i) the integrand in equation (10) varies very strongly as a function of **k** (see for example figure 10) and the entire Brillouin zone has to be considered for integration in order to reproduce the SHC quantitatively correctly; (ii) for the anisotropy of the SHC not only the anisotropy of the wavefunctions with respect to the SQA, discussed in section 3, has to be taken into account, but also the anisotropy of the velocity matrix elements has to be necessarily accounted for. This makes it hardly possible to interpret the spin Hall conductivity in terms of a small number of virtual interband transitions. Even the sign and order of magnitude of the SHC are difficult to predict based on simple arguments.

One aspect we would like to comment on is the importance of transitions in equation (10) which are driven by spin-flip SOC, and the difference between the AHE and SHE as far as the anisotropy of the conductivities is concerned. Let us consider a situation of two doubly degenerate Bloch states

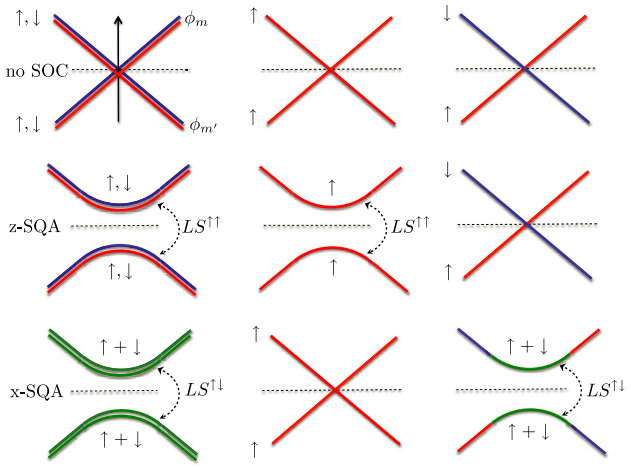

Figure 9. Left column: a band degeneracy due to bands of m and m' orbital character, $|m - m'| \neq 1$, in a paramagnet with structural inversion symmetry without SOC, is lifted due to spin-conserving SOC for SQA along z, and by spin-flip SOC for SQA along x. In a ferromagnet the band degeneracies between the bands of the same spin character (middle column), and of the opposite spin character (right column) have to be considered instead. Note that in this case the energy shifts due to SOC depend strongly on the direction of the magnetization and the type of the crossing. The red (blue) color stands for spin-up (-down) character of the states, while green color marks the states which are of essentially mixed spin character.

at a certain k-point, occupied ψ_n and unoccupied ψ_m. Let us also assume that these states are well separated in energy, i.e., the first-order perturbation theory, as given by equation (17), applies. In this case, consider the contribution to the spin Berry curvature Ω^z_{xy} which comes from the products of the type:

$$\langle\psi_m|v_x\tau_z|\psi_n\rangle\langle\psi_n|v_y|\psi_m\rangle = \langle a^{\uparrow}_m + b^{\downarrow}_m|v_x\tau_z|a^{\uparrow}_n + b^{\downarrow}_n\rangle\langle a^{\uparrow}_n + b^{\downarrow}_n|v_y|a^{\uparrow}_m + b^{\downarrow}_m\rangle,$$

where the SQA is chosen along the z-axis, and $a^{\uparrow}_m = a_m|\uparrow\rangle$, etc, according to the expansion (1). If we neglect the relativistic correction to the velocity operator (as our *ab initio* calculations show it is a very good approximation in most of the cases), the velocity operator does not couple states of different spin and the spin-mixing parameter enters with the terms of the order of $b_m b_n$, which means that the spin-flip spin–orbit appears only in contributions to the spin Berry curvature which are proportional to ξ^2 and higher even powers of ξ (note that ξ is the SOC strength in the system). It is clear that in this case the dominant contribution to the SHC comes from $\sim\xi$ spin-conserving transitions. We prove a similar result in section 5 for the anomalous Hall effect.

While in the largest part of the Brillouin zone the SHC originates mainly from the spin-conserving SOC, in the vicinity of a degeneracy (or crossing) point, such as depicted in figure 9 (left, no SOC), both spin-flip and spin-conserving SOC can provide very large contributions to the SHC. Generally speaking, depending on the orbital character of the states which cross, the role of the spin-conserving and spin-flip SOC for the SHC around such points can be interchanged by changing the SQA. Consider, for example,

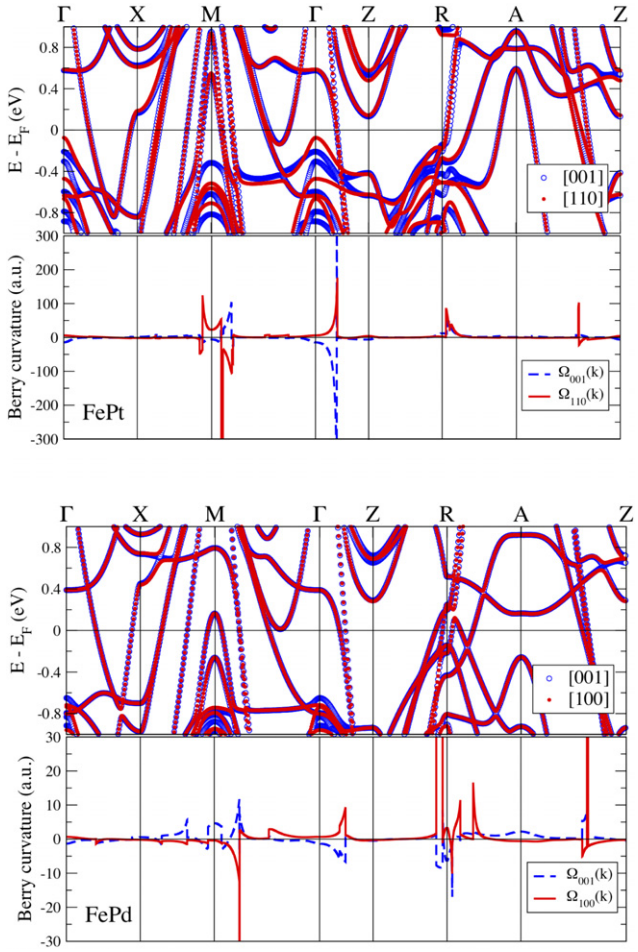

Figure 10. Band structures and distribution of the Berry curvature along high-symmetry directions in the BZ for the magnetization along the [001] and [110] crystallographic axes in $L1_0$ FePt and FePd. Here $\Omega_{[ijk]}$ marks the only non-vanishing component of the Berry curvature vector along the direction of the magnetization $[ijk]$.

a situation from section 3, where the (doubly degenerate) bands which cross have a dominant m and m' orbital character, $|m - m'| \neq 1$, and are well separated from other states, figure 9 (left column). In this case, for the SQA along z, the degeneracy between the states is lifted by $LS^{\uparrow\uparrow}$, and the states keep their almost pure spin character. On the other hand, by pointing the SQA along x, the degeneracy is lifted due to $LS^{\uparrow\downarrow}$, and the states become strongly mixed in spin. Such anisotropy of the wavefunctions will contribute to the anisotropy of the SHC, but what also has to be taken into account is that while in the first case the $v_x\tau_z$ and v_y velocity operators have to be considered in the expression above, in the second case they have to be replaced with $v_y\tau_x$ and v_z. One has to realize that for a k-point away from the high-symmetry directions in the BZ and for the bands which have mixed orbital character the mixture of $LS^{\uparrow\uparrow}$ and $LS^{\uparrow\downarrow}$ in the spin–orbit Hamiltonian can be complicated and the Berry curvature can vary in a non-trivial fashion with the SQA. Nevertheless, by looking at the situation depicted on the left in figure 9, it becomes intuitively clear why the anisotropy of the SHE in paramagnets with structural inversion symmetry is geometric: upon rotation of the SQA, the spin-conserving part of SOC is continuously transformed into the spin-flip part, while the energy spectrum remains unchanged and the crystal basically remains 'the same' system. Indeed, none of the ground state properties of such a crystal are sensitive to the direction of the SQA, and it is the non-equilibrium nature of the spin-relaxation and transport phenomena which makes them sensitive to it. The condition for such a continuous transformation between $LS^{\uparrow\uparrow}$ and $LS^{\uparrow\downarrow}$ obviously lies in the availability of both spin-up and spin-down states for each k-point and energy, i.e., the spin degeneracy.

In a ferromagnet, the spin degeneracy is lifted due to the presence of the magnetization. In this case, since the spin-up and spin-down subspaces are separated in energy, the spin-conserving SOC does not transform continuously into the spin-flip SOC at a given k-point and energy when the magnetization is rotated, and two types of band crossings (or degeneracies) without SOC should be considered: between bands of the same and of opposite spin (see figure 9). Depending on the orbital character of the states, the degeneracy between them will be lifted in the first case by $LS^{\uparrow\uparrow}$ for one direction of the magnetization only (say, z), while in the second case it will be lifted by $LS^{\uparrow\downarrow}$ only for another (say, x), see figure 9. Simply speaking, since the position of the two types of degeneracy in energy and in the Brillouin zone, as well as their number, is different in a ferromagnet, effectively, for the two different directions of the magnetization we have two different systems with a different energy spectrum and different eigenstates. In particular, such asymmetry is the reason for the anisotropy of the orbital moments and total energy in ferromagnets. Since the difference in, e.g., the eigenspectrum for the two different magnetization directions can hardly be reconstructed analytically due to the complexity of the Hamiltonian in transition metals, this leads to a complicated behavior of the AHC as a function of the direction of the magnetization in the crystal. The same holds true for the Elliott–Yafet parameter, considered in section 5, in which case the time-reversal symmetry in the system is effectively broken by a certain spin direction of the injected electrons, which is able to probe the spin-mixing parameter of the states.

Finally, we would like to make two comments. The first one concerns the topology of the degeneracy points in the BZ. The type of degeneracy shown in the upper row of figure 9 provides the so-called *monopole* contribution to the Berry curvature [15], intensively discussed in the literature, especially with respect to topological insulators [55]. Such degeneracies arise at single (often high-symmetry) points in the BZ, as well as along so-called 'hot loops' [32, 79], introduced previously in this review for the case of spin relaxation [36]. Another important contribution to the Berry curvature can also be given by transitions between the pairs of parallel bands degenerate along whole (often high-symmetry) lines or even areas in the BZ—these are the so-called *ladder transitions* [32]. In the language of spin relaxation, such transitions would occur at the spin-flip hot areas in the vicinity of the Fermi surface. The conclusions of the discussion above hold true for both cases. Secondly, it is important to underline that although, referring to the perturbation theory

Table 1. Calculated from first principles, the anomalous Hall conductivity as a function of the direction of magnetization in the crystal. The data are taken from [35] for bcc Fe and hcp Co (similar values for hcp Co were obtained in [17]), from [32, 80] for $L1_0$ FePt and FePd, and from [34] for $L1_0$ CoPt and NiPt. All units are in S cm^{-1}.

	bcc Fe	hcp Co	FePd	FePt	CoPt	NiPt
M ∥ [001]	767	477	135	818	−119	−1165
M ∥ [100]		100				
M ∥ [110]	810		276	409	107	−914
M ∥ [111]	842					

arguments, the same matrix elements of SOC enter into the expressions for energy shifts, Hall conductivities and spin-mixing parameter, these expressions are fundamentally different. This means that, for example, even though the band degeneracy in figure 9 would be lifted by the spin-conserving SOC, it can happen that the major contribution to the Berry curvature is provided by the spin-flip SOC, and the other way around. Concerning this issue, see also the discussion of the second-order perturbation theory expression for the AHC in section 5.2.

5. Anisotropy of intrinsic anomalous Hall effect in metallic ferromagnets

5.1. Anisotropic AHE in uniaxial ferromagnets: first principles studies

Theoretically, the first argument for a strongly anisotropic behavior of the AHC in transition metals was provided by Roman *et al* [17]. In that work it was argued that the main reason for the observed anisotropy of the intrinsic AHC in uniaxial hcp cobalt, which reaches as much as a factor of four between the conductivities for the magnetization in-plane and out-of-plane (see table 1), in agreement with experiment, lies in the irregular and spiky behavior of the Berry curvature in the reciprocal space. In the following, we would like to consider the phenomenon of anisotropic AHE in more detail using first-principles methods. One has to keep in mind that the main conclusions we draw in the following three subsections hold true also for the anisotropic spin Hall effect.

First, let us take a look at the distribution of the Berry curvature along the high-symmetry lines in the Brillouin zone for a typical uniaxial ferromagnet, FePt in the $L1_0$ structure presented in figure 10 (see figure 11(c) for a sketch of the structure and definition of the crystallographic directions). The characteristic spikes in the vicinity of points of near-degeneracy across the Fermi energy can be seen, e.g., around the M-point or in the middle of the ΓZ-path. As we shall see in section 5.2, similarly to the case of the Elliott–Yafet parameter, the large values of the Berry curvature in the vicinity of such points will be inevitably related to the matrix elements of the spin–orbit interaction between the occupied and unoccupied states, scaled by the energy difference between them. As discussed for the case of the EYP and SHE, those matrix elements are strongly anisotropic with respect to the SQA, or, direction of **M**, resulting in the remarkable anisotropy of the Berry curvature in figure 10, both in magnitude (e.g. in the middle of the ΓZ-path) and sign (e.g. close to M-point). When integrated over the whole BZ, the anisotropy of the Berry curvature leads to a factor-of-two reduction in the AHC in FePt as the magnetization is changed from out-of-plane to in-plane (see table 1). In general, in cubic crystals, the anisotropy of the AHE with respect to the directional cosines of the magnetization appears in all odd orders (owing to the anti-symmetry of $\boldsymbol{\sigma}$ with respect to **M**) starting from the third order, and it is normally much weaker than that for the uniaxial crystals, for which the anisotropy is present already in the first order [17], compare e.g. values for bcc Fe to the ones for the uniaxial ferromagnets in table 1.

When we compare the anisotropy of the AHE to the anisotropy of the Elliott–Yafet parameter in metals, several comments can be made. Firstly, the anisotropy of the AHC is a more complex quantity, which hinders analysis in terms of a simple line of arguments, as can be done for the anisotropy of the EYP. This is due to the fact that while for the emergence of the EYP only the spin-flip part of SOC plays a role and the transitions between the spin-degenerate bands can be ignored, for the AHC both spin-conserving and spin-flip parts of SOC have to be taken into account in transitions between occupied and unoccupied bands according to equation (7) (see also considerations at the end of section 4). We analyze this in more detail in the following two subsections. Secondly, in addition to the anisotropy of the SOC matrix elements, similarly to the SHE also anisotropy of the *velocity* matrix elements matters for the total value of the AHC anisotropy. Finally, the Berry curvature is not confined to the Fermi surface, but has a finite spread in energy. While it is already clear from equation (7), in order to further clarify this point we refer to the distribution of the Berry curvature for $L1_0$ FePd alloy in figure 10. In this plot, the presence of wide regions in k-space is evident for which the Berry curvature arises due to transitions between bands which are well separated in energy. Since in such regions the Berry curvature also displays a very anisotropic behavior, it seems reasonable to ask whether there is a certain threshold in energy beyond which the transitions between bands can be neglected for the anisotropy of the AHC.

In order to answer this question, following Roman *et al* [17], we introduce the cumulative anomalous Hall conductivity $A(\omega)$, which accumulates all transitions in equation (7) for which $\varepsilon_{n\mathbf{k}} - \varepsilon_{m\mathbf{k}}$ is larger than $\hbar\omega$. In the limit of $\omega \to 0$ all transitions in equation (7) are accounted for, and $A(\omega = 0)$ equals the full AHC. An inspection of the cumulative AHC presented as a function of energy and magnetization direction in figure 13 (left) for FePt, CoPt and NiPt (the latter two also exhibit a very large anisotropy of the AHC, see table 1), as well as for hcp Co in [17], shows that the energy distribution of transitions which provide the anisotropy of the AHC is concentrated in a narrow 1 eV window around the Fermi energy. This is in contrast to the distribution of $A(\omega)$ for each of the magnetization directions separately, which decays slowly over a much larger energy scale of several eV. We can thus conclude that for the anisotropy of the AHC the

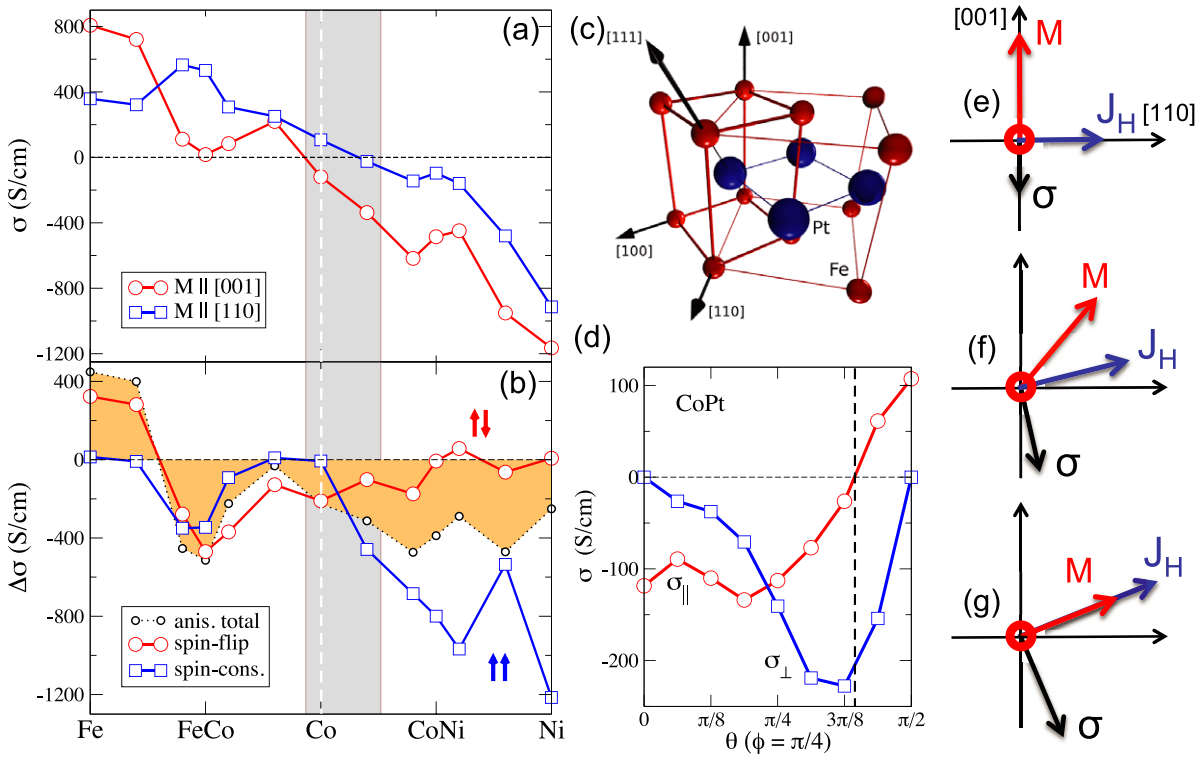

Figure 11. Anomalous Hall conductivity of 3dPt alloys, (a), for **M** along [001] (σ_z, open circles) and [110] (σ_x, open squares), and anisotropy, (b) ($\Delta\sigma^{\text{tot}} = \sigma_z - \sigma_x$, small open circles), with respect to the band filling and within the virtual crystal approximation. (c) Crystal structure of $L1_0$ FePt alloy. Small (red) spheres stand for the Fe atoms, while large (blue) spheres for the Pt atoms. The primitive unit cell used in the calculations is enclosed by thicker lines. In the text, z stands for the [001] axis, while x stands for the [110] direction in the crystal. (d) Anti-ordinary Hall effect in CoPt. Red circles (blue squares) denote the $\sigma_{\parallel}$ ($\sigma_{\perp}$) component of AHC, as a function of the angle θ of the magnetization **M** with the [001]-axis upon rotating it into the [110] direction. (e)–(g) depict the relative orientation of the Hall current $\mathbf{J}_{\text{H}}$, AHC $\boldsymbol{\sigma}$ and magnetization **M** in the situation of the anti-ordinary AHE. In (c)–(e) the magnetization is confined to the $(\bar{1}10)$-plane. We note that, due to symmetry considerations, the conductivity vector stays together with the magnetization in the $(\bar{1}10)$-plane. Taken from [34].

interband transitions in the close vicinity of the Fermi level, which provide very large contribution to the Berry curvature, are more important than for the values of the AHC themselves. This generally agrees with the results for the EYP in Os, figure 6. There, the contributions from the areas where the spin-mixing parameter (Berry curvature in the case of the AHE) was enhanced are dominant for the anisotropy, while for the values of the EYP themselves the regions with smaller spin-mixing parameter are more important, for each of the directions of the SQA.

Generally, the AHC, as well as its anisotropy, displays a strong dependence on the exact position of band degeneracies with respect to the Fermi energy. We therefore expect a non-trivial behavior of the AHC anisotropy for a ferromagnet with a complex electronic structure when the Fermi energy, or other parameters, such as the lattice constant or exchange splitting, are smoothly varied. An example of this phenomenon can be seen in figure 11(a), in which the AHC and its anisotropy are plotted as a function of the band filling in $L1_0$ 3dPt alloys (see section 2 for details of the calculations). In this plot we observe that when going from FePt to NiPt the AHC anisotropy undergoes a change in sign and large changes in magnitude. With the gray shaded area in figure 11(a) the region around the CoPt alloy is highlighted, where both AHC for **M** ∥ [001] (σ_z) and **M** ∥ [110] (σ_x) change their sign. This sign change leads to the occurrence of two key phenomena with respect to the anisotropic AHE. The first one—the *colossal anisotropy* of the AHE—according to calculations in figure 11, occurs for $Fe_xCo_{1-x}Pt$ alloy with $x \approx 0.1$ and for $Co_xNi_{1-x}Pt$ alloy with $x \approx 0.85$. For these two compounds one of the conductivities crosses zero, which marks the complete disappearance of the intrinsic anomalous Hall current $\mathbf{J}_{\text{H}}$ for one of the magnetization directions in the crystal. This is reminiscent of the situation for the spin Hall effect in Ru, see figure 8. In terms of the longitudinal transport within the setup of e.g. anisotropic magnetoresistance experiment [13], the occurrence of the colossal anisotropy of the diagonal conductivity would result in a metal–insulator transition in the crystal—in the case of the colossal AHE anisotropy observed in 3dPt alloys all compounds remain metallic for all magnetization directions, however, and retain their complicated electronic structure around the Fermi energy.

For CoPt alloy the situation, depicted in figures 11(d)–(g), is completely different. Remarkably, $\sigma_{\parallel}$ crosses zero at $\theta_0 = 70°$, which manifests the occurrence of the *anti-ordinary* Hall effect in the crystal of CoPt, discussed already within the framework of the spin Hall effect in section 5.2. At this 'magic' angle, the magnitude of the anomalous Hall current $\mathbf{J}_{\text{H}}$ is almost twice as large as it is for **M** ∥ z, however, due

to the non-vanishing $\sigma_\perp$ component of the AHC vector, $\mathbf{J}_\mathrm{H}$ is aligned *along* the direction of the magnetization. By analyzing figures 11(d)–(g) we observe that the rotational sense of the anomalous Hall current is opposite to that observed in the ordinary Hall effect of the free electron gas. For the ordinary Hall effect, Lorentz forces $\sim[\mathbf{H}\times\mathbf{v}]$ are acting on electrons with velocity $\mathbf{v}$ in the presence of a magnetic field $\mathbf{H}$. The resulting ordinary Hall current of free electrons is always perpendicular to $\mathbf{H}$, irrespective of its direction, opposite to the situation of the anti-ordinary anomalous Hall effect, observed in CoPt. Here, turning the magnetization clockwise in the $(\bar{1}10)$-plane results in an anti-clockwise rotation of $\mathbf{J}_\mathrm{H}$, with its value staying rather large all the time. On the other hand, in analogy to the spin Hall effect, for the anti-ordinary Hall effect, it is possible to find a direction of the electric field $\mathbf{E}$ such that the Hall current is perpendicular to $\mathbf{E}$ and $\mathbf{M}$, which are, in turn, collinear to each other. Again, such a situation obviously cannot occur for the ordinary Hall effect of free electrons.

In 3dPt alloys that are, from an electronic structure point of view, in the vicinity of $L1_0$ CoPt, the anisotropy of the AHE manifests itself in crucial ways, suggesting new functionalities of the AHE-based devices. In these systems, large changes in the magnitude of the anomalous Hall current as well as the relative orientation of the Hall current with respect to the magnetization can be easily achieved by simple reorientation of the sample's magnetization. While the former could be used, for example, to tune the relative magnitudes of the extrinsic and intrinsic anomalous Hall signal [41, 80], among most straightforward applications of the latter could be a realization of the planar Hall effect (PHE) [13, 81], which is related to the Hall effect in ferromagnetic materials with electric field, magnetization and the Hall current sharing same sample plane. So far, it is believed that in most cases the PHE originates from the anisotropic magnetoresistance in metallic ferromagnets, although a PHE mechanism stemming from the anomalous Hall effect due to non-collinearity of the magnetization in semiconductor-based materials has been also suggested [82]. Within the scope of the anti-ordinary Hall effect, described in this work, it would be possible to observe the PHE coming solely from the anisotropic nature of collinear ferromagnetic materials.

5.2. *Perturbation theory treatment: FePt*

In this section we present the perturbation treatment of the intrinsic AHC given by the linear response Kubo formula equation (7). According to first-order non-degenerate perturbation theory, the perturbed wavefunction ψ^σ_m originating from the unperturbed wavefunction $\psi^\sigma_{m,0}$ with spin σ upon including the spin–orbit interaction is given by

$$|\psi^\sigma_m\rangle = |\psi^\sigma_{m,0}\rangle + \sum_{p\neq m;\sigma'} \frac{\langle\psi^{\sigma'}_{p,0}|\xi\mathbf{L}\cdot\mathbf{S}|\psi^\sigma_{m,0}\rangle}{\varepsilon_{m,0}-\varepsilon_{p,0}}|\psi^{\sigma'}_{p,0}\rangle, \quad (27)$$

where $\varepsilon_{m,0}$ and $\varepsilon_{p,0}$ denote the unperturbed eigenenergies, and k-point indices have been omitted for simplicity. Compared to equation (17), here we consider the complete SOC Hamiltonian, and not only its spin-flip part. Following equation (7), in order to obtain an expression for σ_z, the key is to evaluate the imaginary part of the following product:

$$\frac{1}{(\varepsilon^{(1)}_n-\varepsilon^{(1)}_m)^2}\langle\psi^{\sigma'}_n|v_x|\psi^\sigma_m\rangle\langle\psi^\sigma_m|v_y|\psi^{\sigma'}_n\rangle. \quad (28)$$

The energies $\varepsilon^{(1)}_n$ and $\varepsilon^{(1)}_m$ stand for the first-order perturbed eigenvalues. Substituting equation (27) into (28), we can sort out the terms which appear in different orders with respect to the SOC strength ξ. The purpose of this is the general analysis of simplified expressions and discussion of the orders with respect to ξ and their energy scales, which remain valid also when the (degenerate) perturbation theory is applied rigorously in higher orders. In the following we assume that the velocity operator does not contain the relativistic correction due to spin–orbit coupling, which we generally find to be a very good approximation.

A typical first-order contribution to equation (28) involves a sum over additional transitions via auxiliary states $\psi^{\sigma''}_{l,0}$, and looks like:

$$\frac{\xi}{(\varepsilon^{(1)}_n-\varepsilon^{(1)}_m)^2}\langle\psi^{\sigma'}_{n,0}|v_x|\psi^\sigma_{m,0}\rangle \times\sum_{l\neq n;\sigma''}\frac{\langle\psi^{\sigma''}_{l,0}|\mathbf{L}\cdot\mathbf{S}|\psi^{\sigma'}_{n,0}\rangle}{\varepsilon_{n,0}-\varepsilon_{l,0}}\langle\psi^\sigma_{m,0}|v_y|\psi^{\sigma''}_{l,0}\rangle, \quad (29)$$

while the second-order contribution to the product of the matrix elements of the velocity operators involves already two sums of additional transitions via auxiliary states $\psi^{\sigma'''}_{p,0}$ and $\psi^{\sigma''}_{l,0}$, and consists of terms with the following structure:

$$\frac{\xi^2}{(\varepsilon^{(1)}_n-\varepsilon^{(1)}_m)^2}\sum_{p\neq m;\sigma'''}\frac{\langle\psi^{\sigma'''}_{p,0}|\mathbf{L}\cdot\mathbf{S}|\psi^\sigma_{m,0}\rangle}{\varepsilon_{m,0}-\varepsilon_{p,0}}\langle\psi^{\sigma'}_{n,0}|v_x|\psi^{\sigma'''}_{p,0}\rangle \times\sum_{l\neq n;\sigma''}\frac{\langle\psi^{\sigma''}_{l,0}|\mathbf{L}\cdot\mathbf{S}|\psi^{\sigma'}_{n,0}\rangle}{\varepsilon_{n,0}-\varepsilon_{l,0}}\langle\psi^\sigma_{m,0}|v_y|\psi^{\sigma''}_{l,0}\rangle. \quad (30)$$

For the first-order terms, equation (29), the initial state $\psi^\sigma_{m,0}$ and final state $\psi^{\sigma'}_{n,0}$ must have the same spin, since the velocity operator does not act on the spin part of the wavefunction (if we neglect the relativistic correction to the velocity operator). This means that the state $\psi^{\sigma''}_{l,0}$ has to be of the same spin as states n and m. This can happen only due to the spin-conserving part of the spin–orbit interaction $LS^{\uparrow\uparrow}$, as was also found by Cooper [83], meaning that only spin-conserving SOC contributes to the AHC in the first order with respect to ξ. Thus, within the non-degenerate perturbation theory, we would expect the largest contribution to the AHC from the spin-conserving part of the spin–orbit interaction. It should be kept in mind, however, that in materials containing heavy atoms the SOC cannot be treated as a small perturbation. Moreover, as follows from our previous discussion, the important role for the AHC of near-degeneracies across the Fermi level cannot be neglected, for which the above arguments, based on non-degenerate perturbation theory, do not apply (see also discussion at the end of section 4).

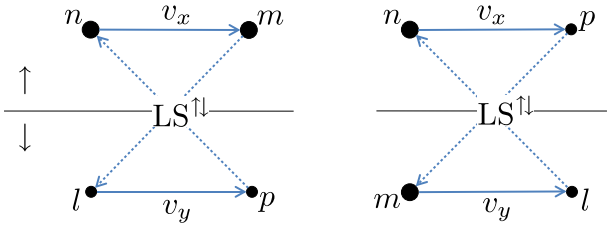

Figure 12. Diagrams depicting the second order in SOC strength ξ contributions to the AHC upon expanding the wavefunctions according to the first-order non-degenerate perturbation theory, see equation (30). The solid (dashed) lines stand for the matrix elements of the velocity operator ($LS^{\uparrow\downarrow}$-operator) between the bra- and ket-states, marked with indices next to the dots, with the direction of the lines from the bra- to the ket-state. The horizontal thin lines separate the $\uparrow$-states from the $\downarrow$-states.

On the other hand, the spin-flip processes contribute only in second- and higher-order terms. We have also come to this conclusion for the spin Hall effect in paramagnets, following a somewhat different argumentation. Analyzing the second order in ξ terms which come from the first-order perturbed wavefunctions, we find four types of contributions to the AHC analogous to the one given by expression (30). All four terms include two summations over auxiliary states $\psi^{\sigma'''}_{p,0}$ and $\psi^{\sigma''}_{l,0}$, and include two products of the matrix elements of the SOC and components of the velocity operator. Assuming for simplicity that the occupied state $\psi^{\sigma'}_{n,0}$ has $\sigma' = \uparrow$, the four types of contributions can be related (omitting the energy denominators for simplicity) to the products of the velocity and SOC matrix elements arranged in the way presented in figure 12. In this figure, the diagram on the left side stands for the product of $\langle\psi^{\uparrow}_{n,0}|v_x|\psi^{\uparrow}_{m,0}\rangle$, $\langle\psi^{\uparrow}_{m,0}|LS^{\uparrow\downarrow}|\psi^{\downarrow}_{l,0}\rangle$, $\langle\psi^{\downarrow}_{l,0}|v_y|\psi^{\downarrow}_{p,0}\rangle$ and $\langle\psi^{\downarrow}_{p,0}|LS^{\uparrow\downarrow}|\psi^{\uparrow}_{n,0}\rangle$, while the diagram on the right side stands for the product of $\langle\psi^{\uparrow}_{n,0}|v_x|\psi^{\uparrow}_{p,0}\rangle$, $\langle\psi^{\uparrow}_{p,0}|\mathrm{LS}^{\uparrow\downarrow}|\psi^{\downarrow}_{m,0}\rangle$, $\langle\psi^{\downarrow}_{m,0}|v_y|\psi^{\downarrow}_{l,0}\rangle$ and $\langle\psi^{\downarrow}_{l,0}|LS^{\uparrow\downarrow}|\psi^{\uparrow}_{n,0}\rangle$. The other two contributions to the second-order AHC come from the diagrams in figure 12, in which the v_x and v_y operators are interchanged, while all directions of the arrows are reversed. As is evident from figure 12, all diagrams contributing to the second-order AHC include the matrix elements of the spin-non-conserving part of the spin–orbit interaction. Interestingly, although a single act of $\mathrm{LS}^{\uparrow\downarrow}$ on a wavefunction is to flip its spin, in addition to the contribution to the AHC from the occupied n and unoccupied m states of different spin character (right diagram), there can also be a non-vanishing contribution from the second-order transition between the n and m states of the same spin.

By calculating the spin–orbit matrix elements in the basis of states unperturbed by SOC, as described in section 2, we applied the non-degenerate first-order perturbation theory in the wavefunctions with respect to SOC and computed the corresponding orders of contributions to the AHC in FePt. The results of these calculations are shown in table 2 for $\mathbf{M} \parallel x$ and $\mathbf{M} \parallel z$. Here, we considered separately the spin-conserving and spin-flip parts of our first-principles Hamiltonian, converged the system, and applied the first-order non-degenerate perturbation theory in wavefunctions, as described above. If we keep only $LS^{\uparrow\uparrow}$ spin–orbit in our calculations, we arrive at the value of the AHC, which we denote as $\sigma^{\uparrow\uparrow}$, while by keeping exclusively the $LS^{\uparrow\downarrow}$ SOC we arrive at the value of the conductivity $\sigma^{\uparrow\downarrow}$. If $\sigma^{\uparrow\uparrow}$ and $\sigma^{\uparrow\downarrow}$ are analogously calculated non-perturbatively from first principles, see right column of table 2, then, as our calculations show (see table 3),

$$\sigma \approx \sigma^{\uparrow\uparrow} + \sigma^{\uparrow\downarrow}, \tag{31}$$

where σ stands for the total AHC calculated with the complete SOC Hamiltonian. Moreover, if the first-order perturbation theory in wavefunctions is applied to evaluate the corresponding conductivities, the above decomposition holds exactly. To obtain the perturbation theory values in table 2, we used a tolerance parameter Δ of 50 meV: that is, when for a considered unperturbed state $|m\rangle$ the difference in energy $|\varepsilon_{m,0} - \varepsilon_{p,0}|$ was less than Δ in equation (27), the projection on state $|p\rangle$ was considered to be zero and the corresponding term in equation (27) was neglected. Overall, by inspecting table 2 we can conclude that the agreement of the perturbation theory results with non-perturbative results presented in tables 1 and 2 for FePt is reasonable. And while this agreement is most probably coincidental for FePt, in which the AHC does not seem to be dominated by singular contributions to the Berry curvature due to transitions between the bands separated by less than 50 meV in energy, nevertheless, certain general features of the spin-flip and spin-conserving AHC apparent from this analysis are universal, as discussed in section 5.3.

Table 2. Decomposition of the AHC of FePt into contributions of different orders and their sum (Σ) based on a perturbative treatment of the spin–orbit interaction, in comparison to first-principles non-perturbative values. All values are in S cm^{-1}. See main text for details.

	1	2	3	4	Σ	Non-perturbative
$\sigma_z^{\uparrow\uparrow}$	581	0	84	0	665	577
$\sigma_z^{\uparrow\downarrow}$	0	84	0	−34	50	133
$\sigma_x^{\uparrow\uparrow}$	557	0	184	0	741	585
$\sigma_x^{\uparrow\downarrow}$	0	−238	0	−106	−344	−184

5.3. *Spin-flip and spin-conserving transitions*

As discussed in section 5.2, and confirmed by explicit calculations within first-order non-degenerate perturbation theory, the spin-conserving part of SOC contributes in first and higher odd orders with respect to the spin–orbit strength, while the spin-non-conserving part of SOC contributes in second and higher even orders. Such oddness and evenness of $\sigma^{\uparrow\uparrow}$ and $\sigma^{\uparrow\downarrow}$ with respect to ξ can also be demonstrated in higher orders of (degenerate) perturbation theory, although we do not provide explicit expressions here. As follows from our calculations, this remains true even when the anomalous Hall conductivity is treated non-perturbatively within the first-principles methods. Here, we present explicit calculations of the $\sigma^{\uparrow\uparrow}$ and $\sigma^{\uparrow\downarrow}$ in $L1_0$ FePt and NiPt as a function of the spin–orbit strength in the system, ξ. The

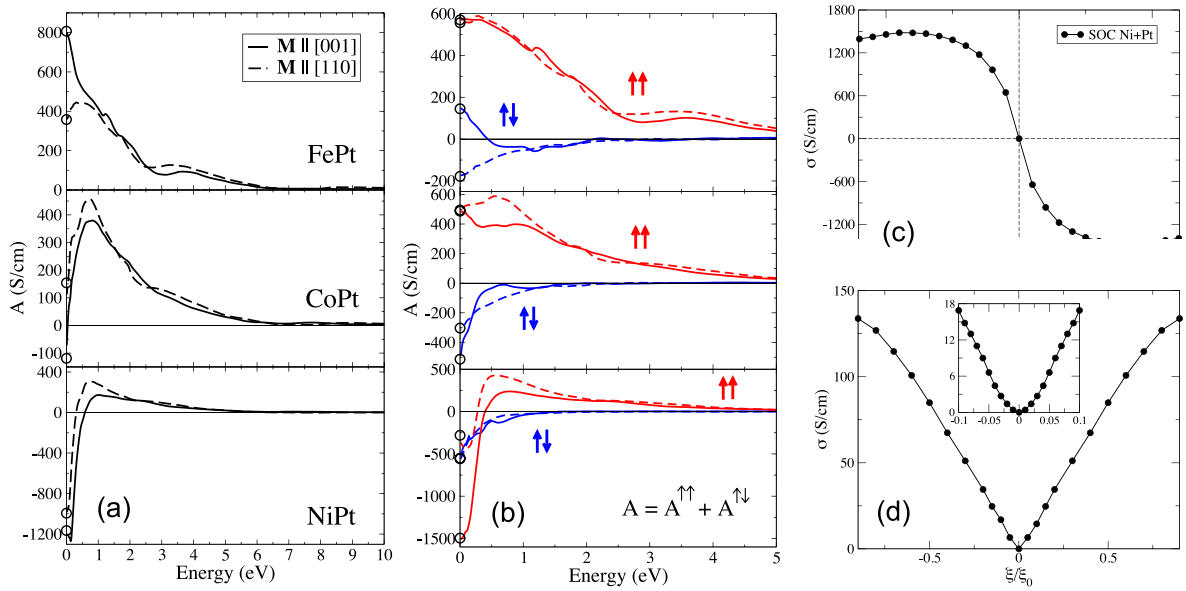

Figure 13. Total (a), spin-conserving ((b), red) and spin-flip ((b), blue) cumulative AHC as a function of energy in FePt, CoPt and NiPt for two different magnetization directions (solid and dashed lines). (c) Scaling of the spin-conserving AHC in NiPt with respect to the strength of spin-conserving SOC on both Ni and Pt sites. (d) Scaling of the spin-flip AHC in FePt with respect to the strength of the spin-flip SOC. SOC on both Fe and Pt sites was scaled uniformly. The inset displays a zoom into the region of small SOC strength. Note that for the sake of this numerical experiment we also consider the regime of negative values of the SOC strength.

Table 3. AHC in FePt for two magnetization directions resolved into spin-flip and spin-conserving contributions from the SOC on each atomic species and compared to the corresponding total values. All values are in S cm^{-1}. Taken from [32].

	σ^{tot}	$\sigma^{\uparrow\uparrow}$	$\sigma^{\uparrow\downarrow}$	Fe^{tot}	$\text{Fe}^{\uparrow\uparrow}$	$\text{Fe}^{\uparrow\downarrow}$	Pt^{tot}	$\text{Pt}^{\uparrow\uparrow}$	$\text{Pt}^{\uparrow\downarrow}$
M ∥ [001]	818	577	133	14	18	−27	848	541	282
M ∥ [100]	409	585	−184	210	254	−38	65	426	−361

results of the calculations, in which the SOC strength was scaled uniformly on 3d and Pt atoms with respect to the unscaled values ξ_0, are presented in figures 13(c) and (d), where we include the non-physical case $\xi < 0$ to demonstrate the even–odd effect. From this plot we observe that, within the accuracy of the calculations, in NiPt the conductivity $\sigma^{\uparrow\uparrow}(\xi) = -\sigma^{\uparrow\uparrow}(-\xi)$, while in FePt $\sigma^{\uparrow\downarrow}(\xi) = \sigma^{\uparrow\downarrow}(-\xi)$, allowing thus for an expansion of $\sigma^{\uparrow\uparrow}(\xi)$ ($\sigma^{\uparrow\downarrow}(\xi)$) in odd (even) powers of ξ. Note also that for larger values of ξ the behavior of $\sigma^{\uparrow\uparrow}$ and $\sigma^{\uparrow\downarrow}$ is manifestly different from linear and quadratic, respectively, marking thus the importance of higher-order terms.

In general, the fact that the spin-conserving transitions appear already in the first order with respect to ξ, while the spin-flip transitions appear in second and higher order, has two essential consequences. Firstly, it means that the energetic spread of the spin-flip conductivity will be much narrower than that of the spin-conserving AHC, due to the higher power of the energy denominator in equation (30) of the order of $(\varepsilon_n - \varepsilon_m)^4$, as compared to that of the order of $(\varepsilon_n - \varepsilon_m)^3$ in equation (29). This can be clearly seen in figure 13(b), in which the cumulative AHC for FePt, CoPt and NiPt is decomposed, analogously to the total AHC, into spin-conserving and spin-flip contributions:

$$A(\omega) \approx A^{\uparrow\uparrow}(\omega) + A^{\uparrow\downarrow}(\omega). \tag{32}$$

Noticeably, while $A^{\uparrow\uparrow}(\omega)$ decays on the scale of the bandwidth of several eV, the spin-flip cumulative AHC is localized in a much narrower energy region, of the order of 1 eV. It is important to mention that the anisotropy of the total AHC can present a competition between the anisotropy of the spin-conserving and spin-flip parts, depending on the exact details of the electronic structure, see for example figures 13(b) and 11(b)—we refer here also to the discussion at the end of section 4.

Remarkably, the energetic scale of the spin-flip transitions in figure 13 roughly corresponds to the energy scale of the spin–orbit interaction of Pt atoms. This observation brings us to the second conclusion that we can make from the perturbation theory analysis: the contribution of spin-conserving transitions to the AHC is normally dominant over the spin-flip transitions (this can be clearly seen in figure 13), since the latter appear only starting from the second order in SOC strength. Correspondingly, in order to promote the spin-flip contribution to the AHC, the spin–orbit strength in the material has to be enhanced. Let us consider this point in detail, and prove that the spin-flip processes in FePt are induced mostly by the strong SOC on the Pt atoms [32]. To do this, we selectively turn off the SOC on each atomic species inside the crystal. The atom-resolved spin–orbit Hamiltonian

reads

$$H_{\mathrm{SO}} = \xi_{\mathrm{Fe}}\mathbf{L}^{\mathrm{Fe}} \cdot \mathbf{S} + \xi_{\mathrm{Pt}}\mathbf{L}^{\mathrm{Pt}} \cdot \mathbf{S}, \tag{33}$$

where $\mathbf{L}^{\mu}$ is the orbital angular momentum operator associated with atomic species μ (Fe or Pt), and ξ_{μ} is the spin–orbit coupling strength averaged over valence d-orbitals. In FePt we find $\xi^0_{\mathrm{Fe}} = 0.06$ eV and $\xi^0_{\mathrm{Pt}} = 0.54$ eV, where ξ^0_{μ} denotes the value calculated from first principles.

Let us recalculate now the AHC after setting to zero either ξ_{Fe} or ξ_{Pt} in equation (33), and then further decompose the conductivity into the spin-flip and spin-conserving parts. The results are presented in table 3. Although such a decomposition is not exact, it reproduces the total values rather well. Namely, the sum of the total conductivities driven by SOC on Fe ($\mathrm{Fe}^{\mathrm{tot}}$ in table 3) and on Pt ($\mathrm{Pt}^{\mathrm{tot}}$ in table 3) is in reasonable agreement with the values of σ^{tot} for both magnetization directions. Moreover, the sum of atom-resolved AHCs into spin-conserving and spin-flip parts is very close to the corresponding total values. Consider first the AHC driven by ξ_{Fe}. For both magnetization directions the spin-flip contribution is very small, while the spin-conserving part is small along [001] but large along [100]. As for the AHC induced by ξ_{Pt}, the spin-conserving part is large but fairly isotropic, while the spin-flip part is highly anisotropic, changing from a large positive value along [001] to a large negative value along [100]. This confirms that the large and strongly anisotropic $\sigma^{\uparrow\downarrow}$ is governed by the SOC inside the Pt atoms.

Let us confirm the conclusion we draw from the perturbation theory description via non-perturbative calculations where we tune by hand the SOC strength ξ_{Pt} on the Pt atoms. The results for the total and spin-flip AHC are shown in figure 14 as a function of $\xi_{\mathrm{Pt}}/\xi^0_{\mathrm{Pt}}$. It can be seen that for ξ_{Pt} less than $\xi^0_{\mathrm{Pt}}/2$, the absolute value of the spin-flip AHC does not exceed a modest value of 50 S cm^{-1}. In this regime σ_z^{tot} and σ_x^{tot} are dominated by spin-conserving processes. Moreover, we note that while the decrease in σ_z^{tot} is almost perfectly linear, σ_x^{tot} stays fairly constant over a wide region of ξ_{Pt} values. This can be understood from the fact that for $\mathbf{M} \parallel x$ the spin-conserving and spin-flip contributions arising from Pt largely cancel one another (see table 3), so that the total AHC is mostly driven by the SOC on the Fe atoms. In contrast, for $\mathbf{M} \parallel z$ it is the SOC on the Pt atoms which dictates the AHC. The artificial tuning of ξ_{Pt} performed above describes rather well what happens if the Pt atoms are replaced with Pd, to form the isoelectronic FePd alloy [80]. This can be seen by comparing the values of σ^{tot} and $\sigma^{\uparrow\downarrow}$ of 135 (276) and 24 (62) S cm^{-1} for $\mathbf{M} \parallel [001]$ ($\mathbf{M} \parallel [100]$), respectively, in FePd with the values taken from the shaded area in figure 14, where $\xi_{\mathrm{Pt}} \approx \xi^0_{\mathrm{Pd}} = 0.19$ eV. In particular, the sign of the AHC anisotropy in FePd, which is opposite from that in FePt, is correctly reproduced by the scaled calculations on FePt.

6. Outlook

In this review we outlined the recent progress in understanding and predicting the anisotropy of the spin-relaxation and intrinsic anomalous and spin Hall effect in metals from first

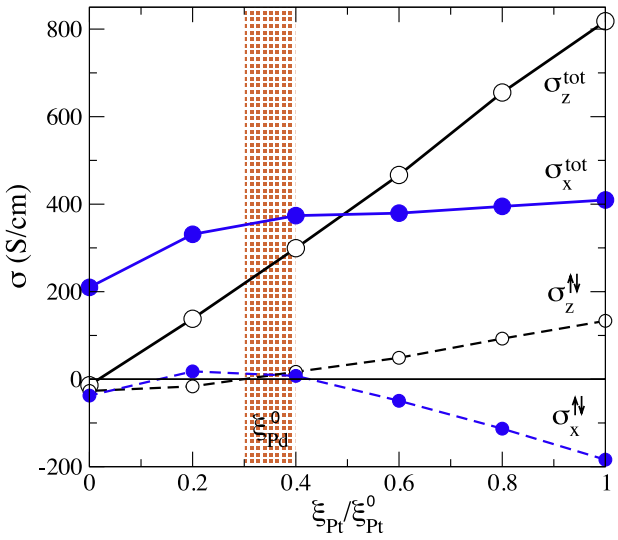

Figure 14. Dependence of the total (σ_z^{tot} and σ_x^{tot}) and spin-flip ($\sigma_z^{\uparrow\downarrow}$ and $\sigma_x^{\uparrow\downarrow}$) AHC in FePt alloy on the strength ξ_{Pt} of the SOC inside the Pt atoms. Reprinted with permission from [32]. Copyright 2011 by the American Physical Society.

principles. In case of the spin relaxation this anisotropy is the consequence of the anisotropy in the wavefunctions upon changing the spin-quantization axis in the crystal, which can be probed via a non-equilibrium process such as an injection of an electron with a certain direction of spin polarization into a material exhibiting an anisotropy of the Elliott–Yafet coefficient. In the case of the spin Hall effect, in addition to the anisotropy of the wavefunctions with respect to the SQA, the anisotropy of the velocity matrix elements comes into play in non-cubic crystals, which leads to an anisotropic correlation between the direction of an applied electric field, direction of the spin current and its spin polarization. For ferromagnets exhibiting the anomalous Hall effect, in addition, eigenvalues and wavefunctions display a very non-trivial dependence on the direction of magnetization in the crystal, which results in a complicated relation between the orientation of magnetization and direction of the Hall current, as well as its magnitude. The anisotropy of the spin-relaxation and Hall currents in perfect crystals can be so strong that it can reach colossal values. For spin and anomalous Hall effects, the magnitude of the Hall current can even be completely suppressed via a suitable choice of the direction of the electric field and/or magnetization. Such strong anisotropy should manifest itself clearly in an experiment, and one of the purposes of the current review is to stimulate further experimental studies with the aim of extending the functionalities of future spintronics devices.

The phenomena considered in this work stem from the electronic structure of perfect idealized solids. In an experiment, especially at finite temperatures, one inevitably faces imperfections in the crystalline order due to impurities or disorder, phonons, magnons etc. For the Hall effects, disorder in the system serves as a source of additional channels for the Hall signal due to so-called skew- and side-jump scattering [84–87]. In the perturbation theory picture, any sort of effects due to impurity scattering should

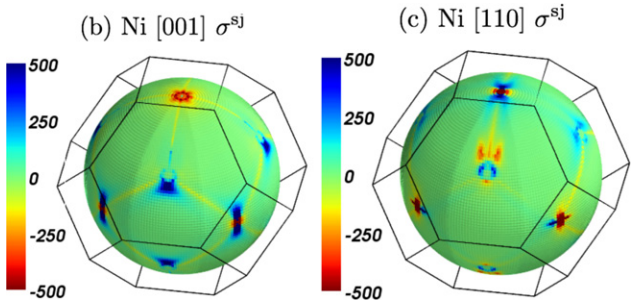

Figure 15. Angle-resolved side-jump conductivity in units of S cm^{-1} as a function of direction in the BZ for fcc Ni for two different magnetization directions. Reprinted with permission from [35]. Copyright 2011 by the American Physical Society.

involve the matrix elements of the scattering potential with the Bloch states of the perfect crystal. And while already the Bloch wavefunctions in the solid, as we discussed, might display an anisotropy with respect to the SQA, also the complicated structure of the impurity potential should exhibit strong anisotropy, due to a possible impurity spin polarization, an internal spin–orbit interaction and an anisotropic crystal field. Recently, assuming a disorder due to point-like delta-correlated defects which do not have any internal structure of the potential, strong anisotropy of the side-jump contribution to the anomalous Hall effect in ferromagnets has been demonstrated from first principles [35] (cf figure 15). In this case the calculated anisotropy is a consequence of the anisotropic electronic structure of the perfect crystal, and the question of the anisotropy of transverse transport due to microscopic details of the impurity potential, which can be treated with high accuracy *ab initio*, still remains open and serves as a fruitful subject for future studies.

Finally, we would like to remark that following the same philosophy, anisotropy of the transverse transport should also be large and experimentally observable for other effects driven by spin–orbit interaction, such as anomalous Nernst effect in ferromagnets [88, 89] and spin Nernst effect in paramagnets [90, 91]. On the other hand, in compounds which exhibit non-collinear magnetic order, the interplay of magnetism and spin–orbit interaction becomes very complex, since the non-collinearity of the local spins can effectively play the role of the spin-flip part of the spin–orbit interaction, and the magnetic ground state itself can be very sensitive to the matrix elements of the spin–orbit interaction. In such a situation, strong anisotropy of the transverse effects observed in this type of systems, such as the magnon Hall effect [92] and the topological Hall effect [93–95], is guaranteed. We are aware only of a single work in this direction [96], while the phenomena mentioned above still remain largely unexplored.

Acknowledgments

We acknowledge funding under DFG project MO 1731/3-1, HGF-YIG program VH-NG-513, and by Grant MAT2012-33720 from the Spanish Ministerio de Economía y Competitividad.

References

[1] Elliott R J 1954 Theory of the effect of spin–orbit coupling on magnetic resonance in some semiconductors *Phys. Rev.* **96** 266–79
[2] Yafet Y 1963 *g* factors and spin–lattice relaxation of conduction electrons *Solid State Physics* vol 14, ed F Seitz and D Turnbull, pp 1–98
[3] Žutić I, Fabian J and Das Sarma S 2004 Spintronics: fundamentals and applications *Rev. Mod. Phys.* **76** 323–410
[4] Karplus R and Luttinger J M 1954 Hall effect in ferromagnetics *Phys. Rev.* **95** 1154–60
[5] Dyakonov M and Perel V 1971 Current-induced spin orientation of electrons in semiconductors *Phys. Lett.* A **35** 459–60
[6] Wang D-S, Wu R and Freeman A J 1993 First-principles theory of surface magnetocrystalline anisotropy and the diatomic-pair model *Phys. Rev.* B **47** 14932–47
[7] van der Laan G 1998 Microscopic origin of magnetocrystalline anisotropy in transition metal thin films *J. Phys.: Condens. Matter* **10** 3239
[8] Bruno P 1989 Tight-binding approach to the orbital magnetic moment and magnetocrystalline anisotropy of transition-metal monolayers *Phys. Rev.* B **39** 865–8
[9] McGuire T and Potter R 1975 Anisotropic magnetoresistance in ferromagnetic 3d alloys *IEEE Trans. Magn.* **11** 1018–38
[10] Bode M, Heinze S, Kubetzka A, Pietzsch O, Nie X, Bihlmayer G, Blügel S and Wiesendanger R 2002 Magnetization-direction-dependent local electronic structure probed by scanning tunneling spectroscopy *Phys. Rev. Lett.* **89** 237205
[11] Gould C, Rüster C, Jungwirth T, Girgis E, Schott G M, Giraud R, Brunner K, Schmidt G and Molenkamp L W 2004 Tunneling anisotropic magnetoresistance: a spin-valve-like tunnel magnetoresistance using a single magnetic layer *Phys. Rev. Lett.* **93** 117203
[12] Velev J, Sabirianov R F, Jaswal S S and Tsymbal E Y 2005 Ballistic anisotropic magnetoresistance *Phys. Rev. Lett.* **94** 127203
[13] Seemann K M, Freimuth F, Zhang H, Blügel S, Mokrousov Y, Bürgler D E and Schneider C M 2011 Origin of the planar Hall effect in nanocrystalline $Co_{60}Fe_{20}B_{20}$ *Phys. Rev. Lett.* **107** 086603
[14] Park B G, Wunderlich J, Williams D A, Joo S J, Jung K Y, Shin K H, Olejnik K, Shick A B and Jungwirth T 2008 Tunneling anisotropic magnetoresistance in multilayer-(Co/Pt)/AlO_x/Pt structures *Phys. Rev. Lett.* **100** 087204
[15] Nagaosa N, Sinova J, Onoda S, MacDonald A H and Ong N P 2010 Anomalous Hall effect *Rev. Mod. Phys.* **82** 1539–92
[16] Fivaz R C 1969 Transport theory for ferromagnets *Phys. Rev.* **183** 586–94
[17] Roman E, Mokrousov Y and Souza I 2009 Orientation dependence of the intrinsic anomalous Hall effect in hcp cobalt *Phys. Rev. Lett.* **103** 097203
[18] Hirsch A and Weissman Y 1973 Anisotropy of the Hall effect in iron *Phys. Lett.* A **44** 239–40
[19] Volkenshtein N, Fedorov G and Shirokovskii V 1961 *Fiz. Met. Metalloved.* **11** 152
[20] Hiraoka T 1968 *J. Sci. Hiroshima Univ.* A-2 **32** 153
[21] Lee R S and Legvold S 1967 Hall effect of gadolinium, lutetium, and yttrium single crystals *Phys. Rev.* **162** 431–5
[22] Ohgushi K, Miyasaka S and Tokura Y 2006 Anisotropic anomalous Hall effect of topological origin in carrier-doped $FeCr_2S_4$ *J. Phys. Soc. Japan* **75** 013710
[23] Sales B C, Jin R and Mandrus D 2008 Orientation dependence of the anomalous Hall resistivity in single crystals of $Yb_{14}MnSb_{11}$ *Phys. Rev.* B **77** 024409

[24] Stankiewicz J and Skokov K P 2008 Anomalous Hall effect in $Y_2Fe_{17-x}Co_x$ single crystals *Phys. Rev.* B **78** 214435

[25] Stankiewicz J, Karpenkov D and Skokov K P 2011 Fundamental magnetotransport anisotropy in R_2Fe_{17} single crystals *Phys. Rev.* B **83** 014419

[26] Sih V, Myers R C, Kato Y K, Lau W H, Gossard A C and Awschalom D D 2005 Spatial imaging of the spin Hall effect and current-induced polarization in two-dimensional electron gases *Nature Phys.* **1** 31–5

[27] Tombros N, Tanabe S, Veligura A, Jozsa C, Popinciuc M, Jonkman H T and van Wees B J 2008 Anisotropic spin relaxation in graphene *Phys. Rev. Lett.* **101** 046601

[28] Averkiev N S and Golub L E 2008 Spin relaxation anisotropy: microscopic mechanisms for 2D systems *Semicond. Sci. Technol.* **23** 114002

[29] Feher G and Kip A F 1955 Electron spin resonance absorption in metals. I. Experimental *Phys. Rev.* B **98** 337–48

[30] Johnson M and Silsbee R H 1985 Interfacial charge–spin coupling: injection and detection of spin magnetization in metals *Phys. Rev. Lett.* **55** 1790–3

[31] Freimuth F, Blügel S and Mokrousov Y 2010 Anisotropic spin Hall effect from first principles *Phys. Rev. Lett.* **105** 246602

[32] Zhang H, Freimuth F, Blügel S, Mokrousov Y and Souza I 2011 Role of spin-flip transitions in the anomalous Hall effect of FePt alloy *Phys. Rev. Lett.* **106** 117202

[33] Chudnovsky E M 2009 Intrinsic spin Hall effect in noncubic crystals *Phys. Rev.* B **80** 153105

[34] Zhang H, Blügel S and Mokrousov Y 2011 Anisotropic intrinsic anomalous Hall effect in ordered 3dPt alloys *Phys. Rev.* B **84** 024401

[35] Weischenberg J, Freimuth F, Sinova J, Blügel S and Mokrousov Y 2011 *Ab initio* theory of the scattering-independent anomalous Hall effect *Phys. Rev. Lett.* **107** 106601

[36] Zimmermann B, Mavropoulos P, Heers S, Long N H, Blügel S and Mokrousov Y 2012 Anisotropy of spin relaxation in metals *Phys. Rev. Lett.* **109** 236603

[37] Fabian J and Das Sarma S 1998 Spin relaxation of conduction electrons in polyvalent metals: theory and a realistic calculation *Phys. Rev. Lett.* **81** 5624–7

[38] Nagaosa N 2006 Anomalous Hall effect: a new perspective *J. Phys. Soc. Japan* **75** 042001

[39] Sinitsyn N A 2008 Semiclassical theories of the anomalous Hall effect *J. Phys.: Condens. Matter* **20** 023201

[40] Gradhand M, Fedorov D V, Zahn P and Mertig I 2010 Extrinsic spin Hall effect from first principles *Phys. Rev. Lett.* **104** 186403

[41] Lowitzer S, Ködderitzsch D and Ebert H 2010 Coherent description of the intrinsic and extrinsic anomalous Hall effect in disordered alloys on an *ab initio* level *Phys. Rev. Lett.* **105** 266604

[42] Yao Y, Kleinman L, MacDonald A H, Sinova J, Jungwirth T, Wang D-S, Wang E and Niu Q 2004 First principles calculation of anomalous Hall conductivity in ferromagnetic bcc Fe *Phys. Rev. Lett.* **92** 037204

[43] Xiao D, Chang M-C and Niu Q 2010 Berry phase effects on electronic properties *Rev. Mod. Phys.* **82** 1959–2007

[44] Gradhand M, Fedorov D, Pientka F, Zahn P, Mertig I and Györffy B 2012 First-principle calculations of the Berry curvature of Bloch states for charge and spin transport of electrons *J. Phys.: Condens. Matter* **24** 213202

[45] Fang Z, Nagaosa N, Takahashi K S, Asamitsu A, Mathieu R, Ogasawara T, Yamada H, Kawasaki M, Tokura Y and Terakura K 2003 The anomalous Hall effect and magnetic monopoles in momentum space *Science* **302** 92–5

[46] Mathieu R, Asamitsu A, Yamada H, Takahashi K S, Kawasaki M, Fang Z, Nagaosa N and Tokura Y 2004 Scaling of the anomalous Hall effect in $Sr_{1-x}Ca_xRuO_3$ *Phys. Rev. Lett.* **93** 016602

[47] Wang X, Yates J R, Souza I and Vanderbilt D 2006 *Ab initio* calculation of the anomalous Hall conductivity by Wannier interpolation *Phys. Rev.* B **74** 195118

[48] Wang X, Vanderbilt D, Yates J R and Souza I 2007 Fermi-surface calculation of the anomalous Hall conductivity *Phys. Rev.* B **76** 195109

[49] Fuh H-R and Guo G-Y 2011 Intrinsic anomalous Hall effect in nickel: A GGA $+U$ study *Phys. Rev.* B **84** 144427

[50] Mikitik G P and Sharlai Y V 1999 Manifestation of Berry's phase in metal physics *Phys. Rev. Lett.* **82** 2147–50

[51] Thouless D J, Kohmoto M, Nightingale M P and den Nijs M 1982 Quantized Hall conductance in a two-dimensional periodic potential *Phys. Rev. Lett.* **49** 405–8

[52] Hasan M Z and Kane C L 2010 Colloquium: topological insulators *Rev. Mod. Phys.* **82** 3045–67

[53] Birss R R 1964 *Symmetry and Magnetism* (Amsterdam: North-Holland)

[54] Hurd C M 1974 *Adv. Phys.* **23** 315

[55] Qi X-L and Zhang S-C 2011 Topological insulators and superconductors *Rev. Mod. Phys.* **83** 1057–110

[56] Hirsch J E 1999 Spin Hall effect *Phys. Rev. Lett.* **83** 1834–7

[57] Kato Y K, Myers R C, Gossard A C and Awschalom D D 2004 Observation of the spin Hall effect in semiconductors *Science* **306** 1910–3

[58] Uchida K, Takahashi S, Harii K, Ieda J, Koshibae W, Ando K, Maekawa S and Saitoh E 2008 Observation of spin Seebeck effect *Nature* **455** 778–81

[59] Liu L, Pai C-F, Li Y, Tseng H W, Ralph D C and Buhrman R A 2012 Spin-torque switching with the giant spin Hall effect of tantalum *Science* **336** 555–8

[60] Murakami S, Nagaosa N and Zhang S-C 2003 Dissipationless quantum spin current at room temperature *Science* **301** 1348–51

[61] Murakami S, Nagaosa N and Zhang S-C 2004 Spin-Hall insulator *Phys. Rev. Lett.* **93** 156804

[62] Bernevig B A, Hughes T L and Zhang S-C 2006 Quantum spin Hall effect and topological phase transition in HgTe quantum wells *Science* **314** 1757–61

[63] König M, Wiedmann S, Brüne C, Roth A, Buhmann H, Molenkamp L W, Qi X-L and Zhang S-C 2007 Quantum spin Hall insulator state in HgTe quantum wells *Science* **318** 766–70

[64] Gradhand M, Fedorov D V, Pientka F, Zahn P, Mertig I and Györffy B L 2011 Calculating the Berry curvature of Bloch electrons using the KKR method *Phys. Rev.* B **84** 075113

[65] Lowitzer S, Gradhand M, Ködderitzsch D, Fedorov D V, Mertig I and Ebert H 2011 Extrinsic and intrinsic contributions to the spin Hall effect of alloys *Phys. Rev. Lett.* **106** 056601

[66] Sinova J, Culcer D, Niu Q, Sinitsyn N A, Jungwirth T and MacDonald A H 2004 Universal intrinsic spin Hall effect *Phys. Rev. Lett.* **92** 126603

[67] Guo G Y, Murakami S, Chen T-W and Nagaosa N 2008 Intrinsic spin Hall effect in platinum: first-principles calculations *Phys. Rev. Lett.* **100** 096401

[68] Shi J, Zhang P, Xiao D and Niu Q 2006 Proper definition of spin current in spin–orbit coupled systems *Phys. Rev. Lett.* **96** 076604

[69] Valenzuela S O and Tinkham M 2006 Direct electronic measurement of the spin Hall effect *Nature* **442** 176

[70] Kampfrath T, Battiato M, Maldonado P, Eilers G, Nötzold J, Radu I, Freimuth F, Mokrousov Y, Blügel S, Wolf M, Oppeneer P M and Münzenberg M 2013 Engineering ultrafast spin currents and terahertz transients by magnetic heterostructures *Nature Nanotechnol.* at press (arXiv:1210.5372 [cond-mat.mes-hall])

[71] Vosko S H, Wilk L and Nusair M 1980 Accurate spin-dependent electron liquid correlation energies for local spin density calculations: a critical analysis *Can. J. Phys.* **58** 1200–11

[72] olymp.cup.uni-muenchen.de/ak/ebert/SPR-TB-KKR
[73] Heers S 2011 *PhD Thesis* RWTH Aachen
[74] www.flapw.de
[75] Souza I, Marzari N and Vanderbilt D 2001 Maximally localized Wannier functions for entangled energy bands *Phys. Rev.* B **65** 035109
[76] Freimuth F, Mokrousov Y, Wortmann D, Heinze S and Blügel S 2008 Maximally localized Wannier functions within the FLAPW formalism *Phys. Rev.* B **78** 035120
[77] Mostofi A A, Yates J R, Lee Y-S, Souza I, Vanderbilt D and Marzari N 2008 Wannier90: a tool for obtaining maximally-localised Wannier functions *Comput. Phys. Commun.* **178** 685–99
[78] Zener C 1954 Classical theory of the temperature dependence of magnetic anisotropy energy *Phys. Rev.* **96** 1335–7
[79] Zhang H, Freimuth F, Bihlmayer G, Blügel S and Mokrousov Y 2012 Topological phases of Bi(111) bilayer in an external exchange field *Phys. Rev.* B **86** 035104
[80] Seemann K M, Mokrousov Y, Aziz A, Miguel J, Kronast F, Kuch W, Blamire M G, Hindmarch A T, Hickey B J, Souza I and Marrows C H 2010 Spin–orbit strength driven crossover between intrinsic and extrinsic mechanisms of the anomalous Hall effect in the epitaxial $L1_0$-ordered ferromagnets FePd and FePt *Phys. Rev. Lett.* **104** 076402
[81] Yau K L and Chang J T H 1971 The planar Hall effect in thin foils of Ni-Fe alloy *J. Phys. F: Met. Phys.* **1** 38
[82] Bowen M, Friedland K-J, Herfort J, Schönherr H-P and Ploog K H 2005 Order-driven contribution to the planar Hall effect in Fe_3Si thin films *Phys. Rev.* B **71** 172401
[83] Cooper B R 1965 Theory of the interband ferromagnetic Kerr effect in nickel *Phys. Rev.* **139** A1504–14
[84] Berger L 1970 Side-jump mechanism for the Hall effect of ferromagnets *Phys. Rev.* B **2** 4559–66
[85] Smit J 1955 The spontaneous Hall effect in ferromagnetics I *Physica* **21** 877–87
[86] Smit J 1958 The spontaneous Hall effect in ferromagnetics II *Physica* **24** 39–51
[87] Sinitsyn N A, Niu Q and MacDonald A H 2006 Coordinate shift in the semiclassical Boltzmann equation and the anomalous Hall effect *Phys. Rev.* B **73** 075318
[88] Miyasato T, Abe N, Fujii T, Asamitsu A, Onoda S, Onose Y, Nagaosa N and Tokura Y 2007 Crossover behavior of the anomalous Hall effect and anomalous Nernst effect in itinerant ferromagnets *Phys. Rev. Lett.* **99** 086602
[89] Xiao D, Yao Y, Fang Z and Niu Q 2006 Berry-phase effect in anomalous thermoelectric transport *Phys. Rev. Lett.* **97** 026603
[90] Cheng S-G, Xing Y, Sun Q-F and Xie X C 2008 Spin Nernst effect and Nernst effect in two-dimensional electron systems *Phys. Rev.* B **78** 045302
[91] Chuu C-P, Chang M-C and Niu Q 2010 Semiclassical dynamics and transport of the Dirac spin *Solid State Commun.* **150** 533–7
[92] Onose Y, Ideue T, Katsura H, Shiomi Y, Nagaosa N and Tokura Y 2010 Observation of the magnon Hall effect *Science* **329** 297–9
[93] Boldrin D and Wills A S 2012 Anomalous Hall effect in geometrically frustrated magnets *Adv. Condens. Matter Phys.* **2012** 615295
[94] Bruno P, Dugaev V K and Taillefumier M 2004 Topological Hall effect and Berry phase in magnetic nanostructures *Phys. Rev. Lett.* **93** 096806
[95] Neubauer A, Pfleiderer C, Binz B, Rosch A, Ritz R, Niklowitz P G and Böni P 2009 Topological Hall effect in the *A* phase of MnSi *Phys. Rev. Lett.* **102** 186602
[96] Balicas L, Nakatsuji S, Machida Y and Onoda S 2011 Anisotropic hysteretic Hall effect and magnetic control of chiral domains in the chiral spin states of $Pr_2Ir_2O_7$ *Phys. Rev. Lett.* **106** 217204